J. Fluid Mech. (2014), *vol.* 746, *pp.* 437–465. © Cambridge University Press 2014
doi:10.1017/jfm.2014.127

A shallow-water sloshing model for wave breaking in rectangular tanks

Matteo Antuono[1,†], Andrea Bardazzi[1], Claudio Lugni[1,2] and Maurizio Brocchini[3]

[1]CNR-INSEAN (Marine Technology Research Institute), via di Vallerano 139, 00128 Rome, Italy

[2]Centre for Autonomous Marine Operations and Systems (AMOS), Department of Marine Technology, NTNU, 7491 Trondheim, Norway

[3]Dipartimento ICEA, Università Politecnica delle Marche, via Brecce Bianche 12, 60121 Ancona, Italy

(Received 12 November 2013; revised 4 February 2014; accepted 3 March 2014; first published online 2 April 2014)

We propose a simple, robust and efficient sloshing model that accounts for breaking phenomena evolving in rectangular tanks and in shallow-water conditions. The model has been obtained by applying Fourier analysis to Boussinesq-type equations and using an approximate analytic solution for the vorticity generated by wave breaking. The toe of the breaker and the intensity of the vorticity injected at the free surface are computed on the basis of literature results for coastal-type breakers. A first experimental campaign has been used to calibrate the turbulent viscosity of the sloshing model, while a second campaign has been run as final validation. The overall good agreement between the numerical outputs and the experimental data confirms the reliability and robustness of the proposed model.

Key words: surface gravity waves, wave breaking, waves/free-surface flows

1. Introduction

Sloshing is a phenomenon that characterizes the liquid inside a tank excited by an external force. Depending on the forcing excitation and on the filling depth, sloshing flows may be very violent, inducing significant global and local loads on the tank walls (see Faltinsen, Landrini & Greco 2004) and increasing the risk for the integrity of the structure. Hence, the study of sloshing is of interest for several branches of engineering, including marine, aerospace and civil engineering. Specifically, it is particularly important for liquified natural gas (LNG) carriers, which must operate in several filling conditions, varying from almost completely to barely filled. For all these reasons, the construction of a model that correctly predicts the sloshing dynamics is very important.

Generally, both analytic and numerical models for sloshing flows only deal with non-breaking waves and, consequently, this significantly restricts their range of applicability. The majority of literature models rely on the use of potential theory (see e.g. Faltinsen *et al.* 2000; Faltinsen & Timokha 2001, 2002; Bredmose *et al.* 2003). Obviously, potential theory is not suited to describe sloshing characterized by rotational flows and, eventually, breaking events. A different approach is possible

† Email address for correspondence: matteo.antuono@cnr.it

https://doi.org/10.1017/jfm.2014.127 Published online by Cambridge University Press

in shallow-water conditions where depth-averaged models are widely used and well established. In this context, a way to describe both breaking phenomena and vorticity dynamics is already available (see Veeramony & Svendsen 2000) and the inclusion of the vortical and turbulent terms in the model equations is straightforward.

The aim of the present work is to extend the model proposed in Antuono *et al.* (2012) (valid for rectangular tanks in shallow-water conditions) to account for wave-breaking events. The model equations are derived from the work of Antuono & Brocchini (2013) and reduce to those of Antuono *et al.* (2012) when waves are non-breaking. In more detail, the proposed scheme relies on the use of a Fourier decomposition to transform the original system of partial differential equations into a system of ordinary differential equations. The approach proposed by Veeramony & Svendsen (2000) has been adapted to this framework and has been used to account for wave breaking and vorticity generation. Specifically, breaking events are detected on the basis of a critical wave slope criterion: where the wave slope exceeds a critical value, the wave is assumed to break, and there vorticity is injected into the liquid as proposed in Veeramony & Svendsen (2000). The injected vorticity becomes the boundary datum at the free surface for the linearized equation of the vorticity. Finally, the analytic solution of the linearized equation is used to evaluate the vortical and turbulent terms inside the model equations. The liquid (which is incompressible and viscous) is assumed to be initially laminar and to become turbulent as a consequence of the breaking events.

Because of the complexity of the phenomena under investigation, some simplifications are necessary. Similarly to the majority of depth-averaged models, a Boussinesq closure has been used for the turbulent terms. Further, the turbulent viscosity has been assumed to be constant all over the liquid domain. This is a simple but reliable and accurate enough approach. In Veeramony & Svendsen's (2000) model, the boundary conditions for the vorticity are assigned along the lower boundary of the 'wave roller' η_e (different from the free surface). Here we simplify this approach and make the assignment directly along the actual free surface, that is, η.

Suitable modelling of wave breaking allows for the study of violent sloshing motions, which cannot be described by the existing modal schemes. In fact, the shallow-water sway cases considered in the present work are characterized by $A^*/h_0^* = O(1)$ (where A^* is the forcing amplitude and h_0^* is the mean water level) while the experiments used to validate the existing models prescribe $A^*/h_0^* < 0.25$ (see e.g. Chester & Bones 1968; Lepelletier & Raichlen 1988; Faltinsen & Timokha 2002). For the roll motion, a straightforward comparison between different experimental campaigns is more difficult, since the dynamics is strongly influenced by the position of the axis of rotation with respect to the centre of mass. The experimental set-up described in the work of Olsen & Johnsen (1975) is fairly similar to the one we use here. However, in that case, the largest roll angle is 0.2°, while in our case the maximum angle is 1°. The largest angles are those in the experiments of Ardakani & Bridges (2012). These have been used to validate a sloshing model built on the nonlinear shallow-water equations. This latter choice allowed a straightforward modelling of the wave breaking but disregards the description of dispersive effects. Because of the use of the nonlinear shallow-water equation, the wave-breaking phenomena are only roughly modelled, lacking a correct description of vorticity injection at the free surface and of turbulence.

Being based on depth-averaged equations, the proposed model is expected to work properly in shallow-water conditions, that is, for $h_0^*/L^* \lesssim 0.1$ (where L^* is the tank length). Specifically, it has been validated for $0.03 \leqslant h_0^*/L^* \leqslant 0.125$, showing a good

https://doi.org/10.1017/jfm.2014.127 Published online by Cambridge University Press

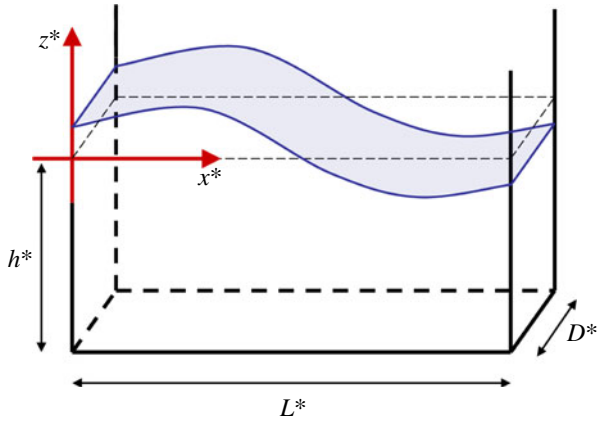


FIGURE 1. (Colour online) Sketch of the tank and the frame of reference.

behaviour also in the lower range of intermediate-depth conditions. Incidentally, we underline that simulations in very shallow depths represent a challenge for sloshing schemes, because of the strong role played by nonlinearities. In these conditions, sloshing models based on potential theory may be affected by convergence problems and/or reduced accuracy (this is reported, for example, in Faltinsen & Timokha (2002) for $h_0^*/L^* < 0.05$).

In summary the model we propose, being based on Fourier analysis, is a very robust, computationally cheap and powerful tool for calculations of sloshing motions characterized by breaking events. Further, its accuracy, already good and largely dependent on the chosen turbulence closures, can eventually be improved by use of more sophisticated closures.

The paper is structured as follows. The next section (§ 2) details the definition of the model. A second part is devoted to the calibrations of the turbulent viscosity (§ 3.2) through a first set of experimental data (§ 3). A third part (§ 3.3) describes the validation of the proposed model and the analysis of its limits of applicability (§ 3.3.1) by means of data collected within a second, specifically designed, experimental campaign. Both experimental campaigns include a variety of breaking events, spreading from bores to plunging breaking waves. Finally, some concluding remarks (§ 4) summarize the essence of the work.

2. Governing equations

Hereinafter, unstarred variables indicate dimensionless quantities, while starred variables indicate dimensional ones. The frame of reference is that of the tank, and x^* and z^* indicate the horizontal and vertical coordinates respectively (see figure 1).

Further, we denote by η_0^* and h_0^* the reference wave amplitude and the mean water depth. Then, the total water depth is given by $d = h + \epsilon\eta$, where ϵ indicates the nonlinearity parameter (i.e. $\epsilon = \eta_0^*/h_0^*$). Because of the scaling, $h = 1$, and it can be neglected in the equations that follow. In any case, we prefer to keep the symbol h to make the derivation of the model straightforward. One second important parameter is $\mu = h_0^*/L^*$, because it measures important features of wave propagation. Specifically, a motion evolves in shallow-water conditions when $\mu \lesssim 0.1$, in intermediate-water conditions for $0.1 \lesssim \mu \lesssim 0.24$, and in deep water for $\mu \gtrsim 0.24$ (see e.g. Faltinsen & Timokha 2002). Since this parameter appears as a multiplicative factor of frequency

https://doi.org/10.1017/jfm.2014.127 Published online by Cambridge University Press

dispersive terms, it is also called the dispersive parameter. Hereinafter, we assume that $\mu \ll 1$, consistent with the shallow-water approximation. Denoting the gravitational acceleration by g^*, the adopted scaling reads

$$x^* = L^* x, \quad z^* = h_0^* z, \quad t^* = \frac{L^*}{\sqrt{g^* h_0^*}}\, t, \quad u^* = \epsilon \sqrt{g^* h_0^*}\, u, \qquad (2.1a,b,c,d)$$

$$\eta^* = \eta_0^* \eta, \quad h^* = h_0^* h, \quad \omega^* = \epsilon \sqrt{\frac{g^*}{h_0^*}}\, \omega, \quad \nu_T^* = \mu h_0^* \sqrt{g^* h_0^*}\, \nu_T, \quad (2.2a,b,c,d)$$

where u^* is the horizontal velocity, ω^* is the vorticity and ν_T^* is the turbulent viscosity. The governing equations of the sloshing model have been obtained from the work of Antuono & Brocchini (2013) by approximating their scheme to the order $O(\epsilon\mu^2, \mu^4)$ (all the details of the derivation may be found in appendix A). They read

$$\begin{cases} \eta_t + (dU)_x = 0, \\ U_t + \epsilon U U_x - F_2(t)\eta_x - \dfrac{\mu^2 h^2}{3} U_{xxt} + \dfrac{\mu^2}{h} \displaystyle\int_{-h}^{\epsilon\eta} \mathrm{d}z \int_z^{\epsilon\eta} \mathrm{d}\zeta \int_\zeta^{\epsilon\eta} R_{xxt}\, \mathrm{d}\xi \\ \quad + \dfrac{\epsilon}{d} \left[\displaystyle\int_{-h}^{\epsilon\eta} R^2\, \mathrm{d}z \right]_x - 4\nu_T \mu^2 U_{xx} - 4\nu_T \dfrac{\mu^2}{h} \displaystyle\int_{-h}^{\epsilon\eta} R_{xx}\, \mathrm{d}z \\ \quad - \nu_T \dfrac{\mu^2}{h} \displaystyle\int_{-h}^{\epsilon\eta} \left[\int_z^{\epsilon\eta} \omega\, \mathrm{d}\zeta \right]_{xx} \mathrm{d}z = M(x) \dfrac{F_1(t)}{\mu} + O(\epsilon\mu^2, \mu^4), \end{cases} \qquad (2.3)$$

where U is the depth-averaged velocity and $M(x)$ is the modulating term described in Antuono *et al.* (2012). The symbols F_1 and F_2, respectively, indicate the horizontal and vertical components of the exciting force and are included inside the governing equations by using the same procedure as described in Antuono *et al.* (2012). The expressions for F_1, F_2 and $M(x)$ are detailed at the end of the present section. The turbulent terms have been expressed through a Boussinesq closure, and the turbulent viscosity, ν_T, has been assumed to be constant in the liquid field. This is a simple but reliable and accurate enough approach. Finally,

$$R = -\int_z^{\epsilon\eta} \omega\, \mathrm{d}\zeta + \frac{1}{d} \int_{-h}^{\epsilon\eta} \mathrm{d}z \int_z^{\epsilon\eta} \omega\, \mathrm{d}\zeta. \qquad (2.4)$$

Following the work of Veeramony & Svendsen (2000), the vorticity is assumed to be known and is modelled through an approximate analytic solution (see appendix A.3 for the details of the computation). Following the work of Antuono *et al.* (2012), we write

$$\eta = \sum_{n=1}^{\infty} H_n(t) \cos(n\pi x), \quad U = \sum_{n=1}^{\infty} U_n(t) \sin(n\pi x), \qquad (2.5a,b)$$

$$\omega = \sum_{n=1}^{\infty} \sum_{m=1}^{\infty} \phi_{n,m}(t) \sin(n\pi x) \sin(m\pi y) \quad \text{with } y = -\frac{\epsilon\eta - z}{d}. \qquad (2.6)$$

The variable y is used to simplify the assignment of the vorticity injection at the free surface. These expressions are rewritten by using complex numbers as follows:

$$\eta = \sum_{n\in\mathbb{Z}} \frac{H_n(t)}{2}\, \mathrm{e}^{\mathrm{i}n\pi x}, \quad U = \sum_{n\in\mathbb{Z}} \frac{U_n(t)}{2\mathrm{i}}\, \mathrm{e}^{\mathrm{i}n\pi x}, \qquad (2.7a,b)$$

$$\omega = \sum_{n\in\mathbb{Z}} \frac{\mathrm{e}^{\mathrm{i}n\pi x}}{2\mathrm{i}} \sum_{m=1}^{+\infty} \phi_{n,m} \sin(m\pi y), \qquad (2.8)$$

https://doi.org/10.1017/jfm.2014.127 Published online by Cambridge University Press

with $H_{-n} = H_n$, $U_{-n} = -U_n$ and $\phi_{-n,m} = -\phi_{n,m}$ for all $m \in \mathbb{Z}$. The use of Fourier series to describe the flow quantities even for breaking events is possible because we use depth-averaged equations. In this context, the free surface (as well as the remaining flow variables) is always single-valued and, in the occurrence of breaking events, it represents a mean surface elevation. The wave breaking and the vorticity injection at the free surface are then modelled by using *ad hoc* models (as described in appendices A.2 and A.3).

Substituting the above expressions into the system (2.3) and dropping all terms that are $O(\epsilon\mu^2, \mu^4)$, we obtain

$$\begin{cases} \dot{H}_n + n\pi h U_n + \epsilon \dfrac{n\pi}{4} \displaystyle\sum_{p\in\mathbb{Z}} [H_p U_{n-p} + H_{n-p} U_p] = 0, \\ \dot{U}_n \left(1 + \dfrac{\mu^2 n^2 \pi^2 h^2}{3}\right) + n\pi F_2 H_n + \beta_n U_n + \epsilon \dfrac{n\pi}{4} \displaystyle\sum_{p\in\mathbb{Z}} U_p U_{n-p} + \mu^2 n^2 \pi^2 \sum_{m=1}^{+\infty} \frac{\dot{\phi}_{n,m}}{(m\chi)^3} \\ \quad + \epsilon \dfrac{n\pi}{4} \displaystyle\sum_{p\in\mathbb{Z}} \sum_{m=1}^{+\infty} \frac{\phi_{p,m}\phi_{n-p,m}}{(m\chi)^2} + 4\nu_T \mu^2 n^2 \pi^2 U_n - \nu_T \mu^2 n^2 \pi^2 \sum_{m=1}^{+\infty} \frac{\phi_{n,m}}{(m\chi)} = M_n \frac{F_1}{\mu}, \end{cases} \tag{2.9}$$

where $\chi = \pi/h$ is the (dimensionless) wavenumber associated with the vertical direction and

$$\beta_n = \left(1 + \frac{2h^*}{D^*}\right) \left(\frac{\nu n \pi}{2h\sqrt{h}}\right)^{1/2} + 4\nu\mu^2 n^2 \pi^2, \tag{2.10}$$

where $\nu = \nu^*/(\mu h_0^* \sqrt{g^* h_0^*})$ is the dimensionless kinematic viscosity of the liquid and D^* is the tank breadth. As explained in Antuono *et al.* (2012), the coefficient β_n takes into account the dissipation caused by the boundary layer along the tank wall and the viscous dissipation inside the liquid bulk (see e.g. Lamb 1945; Antuono & Colagrossi 2013). In particular, the term $(4\nu_T \mu^2 n^2 \pi^2 U_n)$ represents the dissipation due to turbulence. In any case, since turbulence is generated by wave breaking, this term is switched on only when breaking occurs. Otherwise, it is set to zero.

Before proceeding to the analysis, we briefly recall the expressions for the forces F_1 and F_2. These have been derived in Antuono *et al.* (2012) and are very similar to the Lukovsky formulas (see e.g. Faltinsen & Timokha 2009). Denoting the tank acceleration by $a_0 = (a_{0,1}, a_{0,2}, 0)$ and its rotation by $R = (0, 0, \dot{\theta})$ (here θ is the angle between the horizontal axis of the frame of reference of the tank and the horizontal axis of the fixed frame of reference), we have

$$F_1(t) = -\sin\theta - a_{0,1}\cos\theta - a_{0,2}\sin\theta + \mu^2 \ddot{\theta}(z_C - z_0) + \mu\dot{\theta}^2(x_C - x_0) + 2\mu^2 \dot{\theta} w_C, \tag{2.11}$$

$$F_2(t) = -\cos\theta + a_{0,1}\sin\theta - a_{0,2}\cos\theta - \mu\ddot{\theta}(x_C - x_0) + \mu^2\dot{\theta}^2(z_C - z_0) - 2\mu\dot{\theta} u_C. \tag{2.12}$$

Here, x_C and z_C are the coordinates of the centre of mass of the tank, u_C and w_C its velocity components, and x_0 and z_0 the coordinates of the centre of rotation. Specifically,

$$x_C^* = L^* \left\{ \frac{1}{2} + \sum_{n=1}^{+\infty} \frac{[-1 + (-1)^n]}{\pi^2 n^2} \frac{H_n^*(t^*)}{h_0^*} \right\}, \quad z_C^* = h_0^* \left\{ -\frac{1}{2} + \sum_{n=1}^{+\infty} \left[\frac{H_n^*(t^*)}{2h_0^*}\right]^2 \right\}, \tag{2.13a,b}$$

https://doi.org/10.1017/jfm.2014.127 Published online by Cambridge University Press

while the centre-of-mass velocity is simply given by the time derivative of the centre-of-mass position,

$$u_C^* = L^* \sum_{n=1}^{+\infty} \frac{[-1+(-1)^n]}{\pi^2 n^2} \frac{\dot{H}_n^*(t^*)}{h_0^*}, \quad w_C^* = \sum_{n=1}^{+\infty} \frac{H_n^*(t^*)}{2h_0^*} \dot{H}_n^*(t^*). \tag{2.14a,b}$$

At each time step we first integrate the continuity equation and find $\dot{H}_n^*$ for each n, and then we use these solutions to update the centre-of-mass velocity and integrate the momentum equation. Finally, the argument of the modulating term is given by

$$M_n = -2\left[\frac{(-1)^n - 1}{n\pi}\right] \quad \text{for } n \in \mathbb{Z} \setminus \{0\}, \;\; M_0 = 0. \tag{2.15a,b}$$

More details can be found in Antuono *et al.* (2012).

Hereinafter the proposed model is referred to as the 'modal system' or 'modal method', because of its similarity to the multi-modal schemes generally used for the analysis of sloshing phenomena (e.g. Faltinsen *et al.* 2000; Faltinsen & Timokha 2002; Hill 2003). In any case, the procedure used to obtain system (2.9) is somewhat different from that used in the models of Faltinsen *et al.* (2000) and Faltinsen & Timokha (2002). Those rely on an estimate of the mode magnitude and on a subsequent truncation (the reference parameter is $\varepsilon = A^*/h_0^*$). In the proposed model, we do not give any estimate but retain a large enough number of modes to describe the wave focusing and breaking.

3. Applications

The analysis that follows is divided into two parts. In the first one we use numerical solutions and experimental measurements to calibrate the turbulent viscosity of the proposed model. The experimental data are those of the campaign described in Bouscasse *et al.* (2013), while the numerical solutions have been obtained by using the δ-SPH (smoothed particle hydrodynamics) model proposed in Antuono *et al.* (2011). In the second part, we deal with the validation of the model. For this purpose, a novel specific experimental campaign has been carried out.

The sloshing phenomenon is characterized by natural frequencies of oscillation. These are derived by using the linear theory as a first-order approximation and read

$$\sigma_{r,n}^* = \sqrt{g^* n k^* \tanh(n k^* h^*)}, \quad n = 1, 2, 3, \ldots, \tag{3.1}$$

where $k^* = \pi/L^*$ is the wavenumber associated with the tank dimension. For ease of notation, the lowest natural frequency (that is, $n = 1$) is denoted by σ_r^*. A violent surface-wave response may take place when the forcing frequency is close to σ_r^*, regardless of the forcing amplitude. This resonant excitation ceases at a critical frequency σ_b^* close to σ_r^* due to a bifurcation phenomenon explained in Faltinsen *et al.* (2000). Resonance arises also around higher natural frequencies (that is, $n > 1$) even if these, generally, induce a weaker wave response.

Depth-averaged models (like the present one) and asymptotic shallow-water modal schemes (e.g. Faltinsen & Timokha 2002) generally predict linear dispersion relations that differ from the exact one and provide a good approximation only in shallow- and intermediate-water conditions. In any case, all the sloshing experiments and simulations shown in the present work are within such a range.

https://doi.org/10.1017/jfm.2014.127 Published online by Cambridge University Press

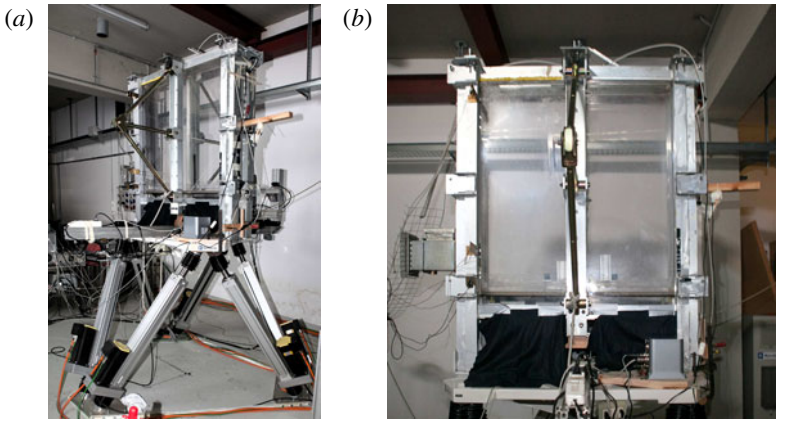


FIGURE 2. (Colour online) The experimental set-up.

3.1. *CNR-INSEAN experimental set-up*

The tank used during the experimental campaigns at CNR-INSEAN is $L^* = 1$ m long and $D^* = 0.1$ m wide, and is filled with water up to a height h^* (see sketch of figure 1). The geometry of the tank, i.e. $D^*/L^* = 0.1$, ensures an almost two-dimensional (2D) flow in the main tank plane. The experimental set-up is shown in figure 2.

The first experimental campaign is that described in Bouscasse *et al.* (2013). Three capacitance wave probes are placed at the sides of the tank. The first one η_1^* is positioned at a distance of 1 cm from one side, the second one η_5^* at distance of 5 cm and the third one η_{50}^* at the middle of the tank. During the tests, flow visualizations have been performed through a digital video camera (JAI CV-M2). This camera has a spatial resolution of 1600×1200 pixels and frequency rate equal to 15 Hz. It has been placed in front of the tank and sufficiently far from it to record the global behaviour of the propagating wave. Finally, a wire potentiometer has been used for a direct measurement of the position of the tank. Particular care has been devoted to the synchronization of the several acquisition systems with different sampling rates, used for the recording of the signals.

For the second campaign, a solution of water and fluorescein has been used to trace the evolution of the free surface. The experiment has been conducted in a darkened room, and the fluorescein solution has been excited by using five blue light-emitting diodes (LEDs) (480 nm, 3 W) placed at a regular distance below the tank bottom. The flow evolution has been recorded through two cameras (Falcon 1.4M100 Dalsa) with a spatial resolution of 1400×1024 pixels and frequency rate equal to 100 frames per second. The free surface has been detected by using an in-house code for image analysis.

For the tank motion, an *ad hoc* mechanical system has been used. Specifically, we considered a sinusoidal motion for both sway and roll cases with an initial ramp, to avoid an impulsive start – see Antuono *et al.* (2012) for more details. When the ramp ceases, the sway and roll forcing are respectively given by

$$x^*_{tank}(t) = A^* \sin(\sigma^* t^*), \quad \theta(t) = \theta_0 \sin(\sigma^* t^*), \tag{3.2a,b}$$

where σ^* is the angular frequency, A^* is the displacement amplitude and θ_0 is the angle (in radians) between the horizontal axis in the frame of reference of the tank and that of the Earth. The centre of rotation is set in the middle of the tank bottom.

https://doi.org/10.1017/jfm.2014.127 Published online by Cambridge University Press

	A^*/h_0^*	h_0^*/L^*	σ_r^* (s^{-1})	σ^*/σ_r^*	Motion regime	Breaking type
Series 1	0.500	0.060	2.3961	0.874, 1.192	Weak/moderate	Bore/plunging
Series 2	0.800	0.125	3.3936	1.00	Strong	Plunging
Series 3	2.333	0.030	1.7018	1.230, 2.307	Strong/weak	Plunging/bore

TABLE 1. The first experimental campaigns considered in the present work.

3.2. *Calibration of the turbulent viscosity*

From the first experimental campaign, we consider three configurations of sway motions in shallow-water conditions. These are summarized in table 1, and, once a steady state has been reached, they are all characterized by breaking waves. Specifically, moderate breaking events occur in Series 1 while strong breaking waves are generated in Series 2 and 3. The modal method has been implemented by using 200 modes in the x direction and 50 along the vertical direction. All the results may be taken as converged ones.

The main mechanism of energy dissipation is related to the turbulent terms and, consequently, to the value of the turbulent viscosity. According to Cox, Kobayashi & Okayasu (1995), the turbulent viscosity in the shallow-water regime has to vary in the following interval:

$$\nu_T^* = \mu \nu_T h_0^* \sqrt{g^* h_0^*} \simeq (0.03\text{–}0.04) h_0^* \sqrt{g^* h_0^*}. \tag{3.3}$$

The above formula has been derived for coastal flows, but the sloshing simulations that implement ν_T^* in such a range appear to be somewhat too energetic in comparison to experimental data and SPH simulations. Then, we analyse the sloshing model by varying ν_T^* over a wider range (specifically, $\mu\nu_T = 0.03, 0.06, 0.09, 0.12$) and compare the results with both the δ-SPH scheme and the experimental measurements.

The first case is Series 1 with $\sigma^* = 2.094$ s^{-1} (i.e. $\sigma^*/\sigma_r^* = 0.874$, see figure 3). Breaking events are very weak and, consequently, only minor differences are observed on varying ν_T. The overall match with the δ-SPH and the experiments is very good. Figure 4 shows the results obtained with the same configuration (Series 1) and $\sigma^* = 2.856$ s^{-1} (i.e. $\sigma^*/\sigma_r^* = 1.192$). In this case, breaking events are stronger and the action of turbulent terms is more evident. Specifically, the trough between the two highest peaks of the signal tends to reduce as ν_T increases. Again, the overall match with the δ-SPH and the experiments is good.

The second case is more problematic and is described in figure 5 (Series 2, $\sigma^* = 3.393$ s^{-1}, $\sigma^*/\sigma_r^* = 1$). Here, breaking events are very intense and both the δ-SPH and the experimental data are characterized by a sawtooth signal. For $\nu_T = 0.03/\mu$ and $0.06/\mu$, the turbulent terms are too weak and a two-peak signal is obtained. Conversely, a good agreement is obtained for $\nu_T = 0.09/\mu$ and $0.12/\mu$, even if the last case does seem a bit too dissipative.

The last configuration (Series 3) is the most energetic. Figure 6 shows the test with $\sigma^* = 2.094$ s^{-1} (i.e. $\sigma^*/\sigma_r^* = 1.230$, very close to bifurcation). In this case, the proposed model cannot dissipate enough energy through wave breaking and the solution is that of a typical undular bore, i.e. made of wave trains with large oscillations. An increase in ν_T reduces these oscillations, with a consequent improvement of the agreement, but cannot completely dissipate them. We anticipate that this behaviour generally characterizes those simulations with large values of A^*/h_0^* and small values of $\mu = h_0^*/L^*$. A more detailed analysis is given in § 3.3.1.

https://doi.org/10.1017/jfm.2014.127 Published online by Cambridge University Press

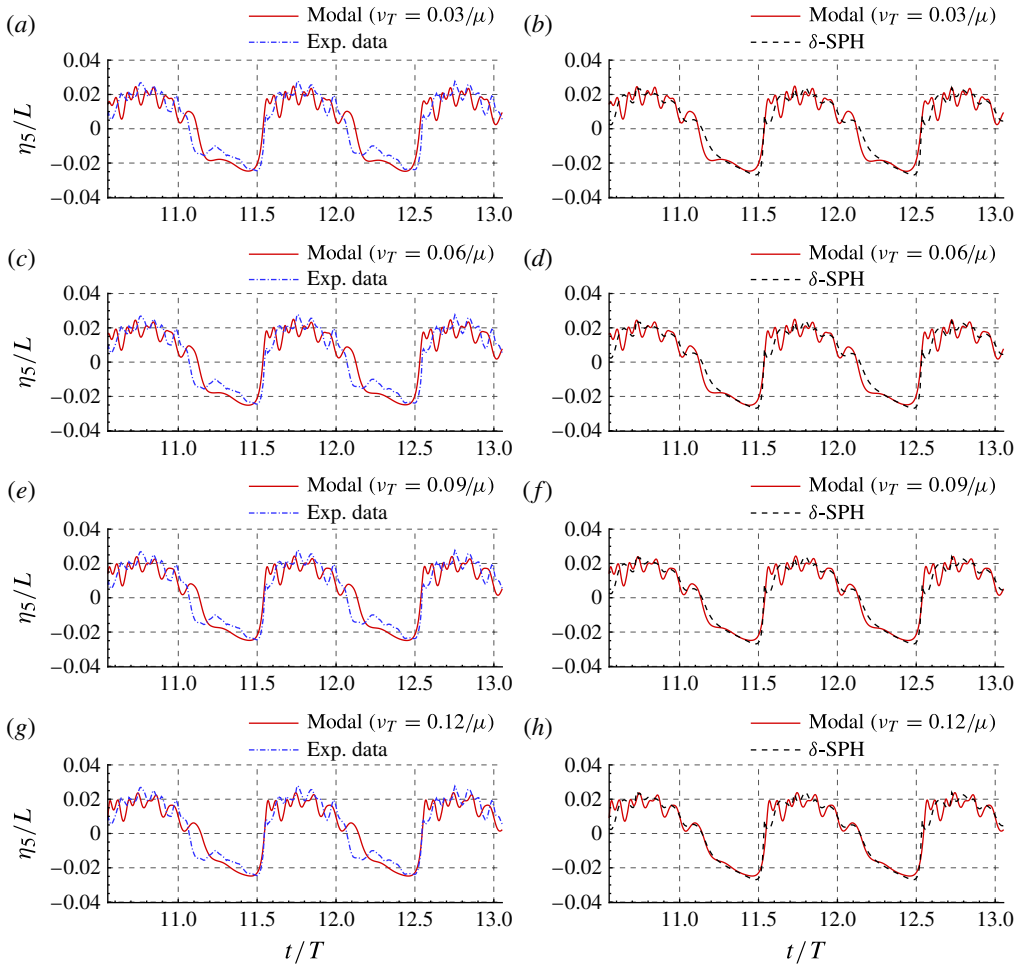


FIGURE 3. (Colour online) Series 1, $\sigma^* = 2.094$ s^{-1} ($\sigma^*/\sigma_r^* = 0.874$), and $x^*/L^* = 0.05$.

One further interesting case is represented by Series 3 with $\sigma^* = 3.927$ s^{-1} (i.e. $\sigma^*/\sigma_r^* = 2.307$). In this case, the frequency is beyond the bifurcation point (close to the second natural frequency of oscillation) and the dynamics is not very strong. The free-surface signal is 'asymmetric', that is, the signal measured at $x^*/L^* = 0.05$ is not a simple temporal translation of the signal measured at $x^*/L^* = 0.95$. The comparison for different values of ν_T is shown in figures 7–10. Apart from the last case ($\nu_T = 0.12/\mu$), the modal method predicts an asymmetric behaviour of the free-surface signal. However, the signal for $\nu_T = 0.03/\mu$ is too energetic and, further, does not predict the doubly periodic modulation that characterizes the experimental measurements and the δ-SPH results at $x^*/L^* = 0.05$. On the contrary, the signals obtained by using $\nu_T = 0.06/\mu$ (figure 8) and $\nu_T = 0.09/\mu$ (figure 9) show a good agreement with both the δ-SPH results and the experiments. The above analysis suggests that a suitable choice for the turbulent viscosity for sloshing problems is

$$\nu_T^* = \mu \nu_T h_0^* \sqrt{g^* h_0^*} \simeq (0.06\text{–}0.09) h_0^* \sqrt{g^* h_0^*}. \tag{3.4}$$

Specifically, we choose $\nu_T = 0.08/\mu$ for the numerical simulations of § 3.3.

https://doi.org/10.1017/jfm.2014.127 Published online by Cambridge University Press

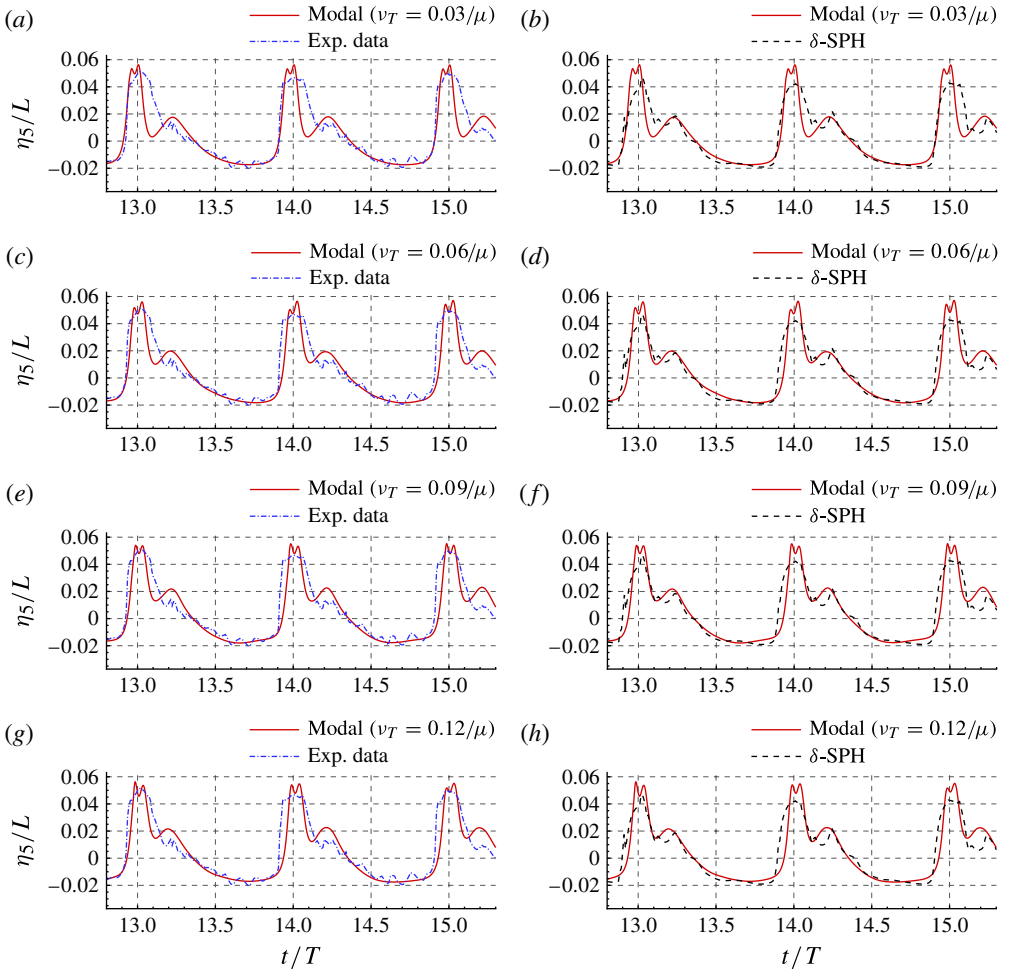


FIGURE 4. (Colour online) Series 1, $\sigma^* = 2.856$ s^{-1} ($\sigma^*/\sigma_r^* = 1.192$), and $x^*/L^* = 0.05$.

We here underline that the model proposed in Antuono *et al.* (2012) (which does not account for wave breaking) cannot describe the test cases shown up to here. In fact, lacking the dissipation mechanisms due to the vorticity and turbulence, it is affected by large spurious oscillations that make the simulations unstable.

3.3. *Validation*

In this section we deal with the validation of the proposed model. This has been carried out on the basis of the data collected through the second experimental campaign described in § 3.1, in which both sway and roll motions have been accounted for. The filling configurations are briefly summarized in tables 2 and 3, and include both moderate and strong motion regimes, varying from very shallow depths ($h_0^*/L^* = 0.034$) to almost intermediate depths ($h_0^*/L^* = 0.089$). The comparison between the numerical outputs and the experimental measurements has been done on the basis of the free-surface evolution at four locations, namely $x^*/L* = 0.05,\ 0.1,\ 0.2,\ 0.3$, and at fixed time instants (all over the tank width). We start by describing the cases in deeper water, and we leave the cases with $h_0^*/L^* = 0.034$ to the end of our discussion, since these deserve a more detailed analysis.

https://doi.org/10.1017/jfm.2014.127 Published online by Cambridge University Press

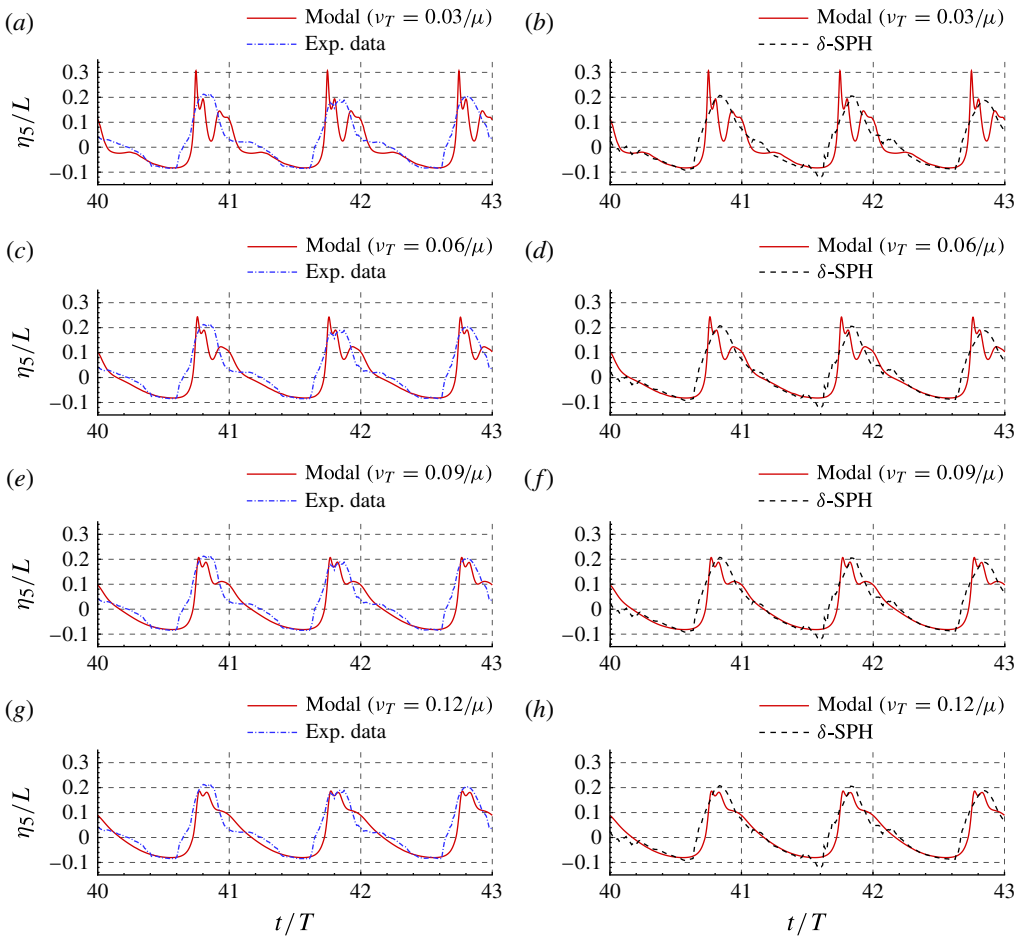


FIGURE 5. (Colour online) Series 2, $\sigma^* = 3.393$ s^{-1} ($\sigma^*/\sigma_r^* = 1$), and $x^*/L^* = 0.05$.

Sway	A^*/h_0^*	h_0^*/L^*	σ_r^* (s^{-1})	σ^*/σ_r^*	Motion regime	Breaking type
Series S1	1.00	0.034	1.8178	1.25	Moderate	Bore
Series S2	1.00	0.069	2.6052	1.10	Strong	Plunging
Series S3	0.60	0.089	2.9745	0.95	Strong	Plunging

TABLE 2. The second experimental campaigns. The sway motion.

The first case is a sway motion at $h_0^*/L^* = 0.089$ with $\sigma^*/\sigma_r^* = 0.95$ (Series S3). This is characterized by a strong dynamics with violent breaking events, which develop in the form of travelling bores. The free surface predicted by the model is compared with the experiments in figure 11 at fixed positions. At $x^*/L^* = 0.05$ (figure 11*a*) both the experimental and numerical signals are characterized by a sawtooth profile, which is typical for a travelling bore. At $x^*/L^* = 0.1$ (figure 11*b*) the signals display secondary peaks, which become more pronounced at $x^*/L^* = 0.2,\ 0.3$ (figure 11*c*,*d*). The overall match is good even if a careful analysis of these signals shows that the experimental

https://doi.org/10.1017/jfm.2014.127 Published online by Cambridge University Press

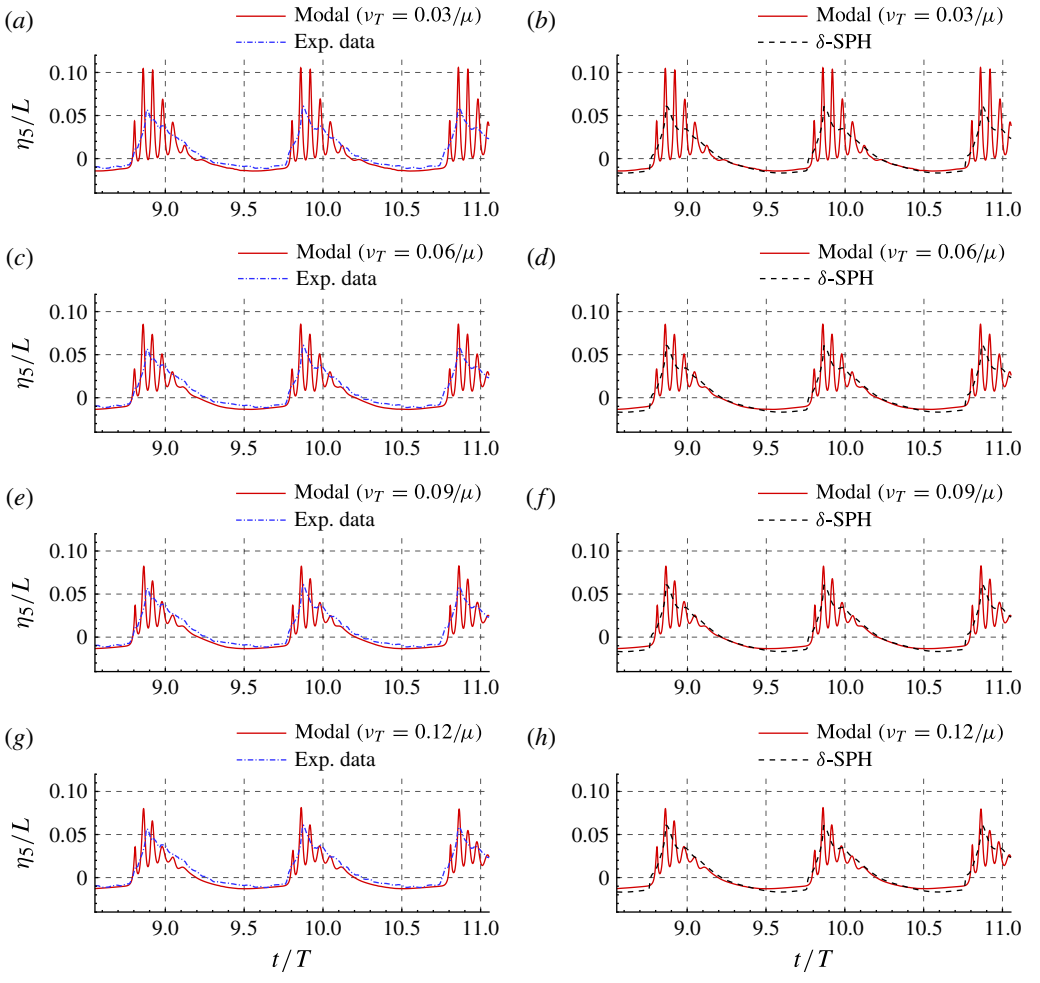


FIGURE 6. (Colour online) Series 3, $\sigma^* = 2.094$ s^{-1} ($\sigma^*/\sigma_r^* = 1.230$), and $x^*/L^* = 0.05$.

Roll	θ (rad)	h_0^*/L^*	σ_r^* (s^{-1})	σ^*/σ_r^*	Motion regime	Breaking type
Series R1	$\pi/180$	0.034	1.8178	1.20	Moderate	Bore
Series R2	$\pi/180$	0.069	2.6052	1.00	Strong	Bore
Series R3	$\pi/180$	0.089	2.9745	1.10	Strong	Bore

TABLE 3. The second experimental campaigns. The roll motion.

data (which are synchronous with the numerical ones at $x^*/L^* = 0.05$, that is, close to the wall) tend to slightly anticipate the numerical outputs at $x^*/L^* = 0.2$, 0.3. This phenomenon can be easily explained by looking at the global free-surface evolution. Figure 12 displays some snapshots of the free-surface evolution along with the contour of vorticity field as predicted by the proposed model. The black solid lines represent the experimental data. The numerical and experimental free surfaces are initially in synchronization close to the right wall (figure 12*a*,*b*). As the wave moves towards

https://doi.org/10.1017/jfm.2014.127 Published online by Cambridge University Press

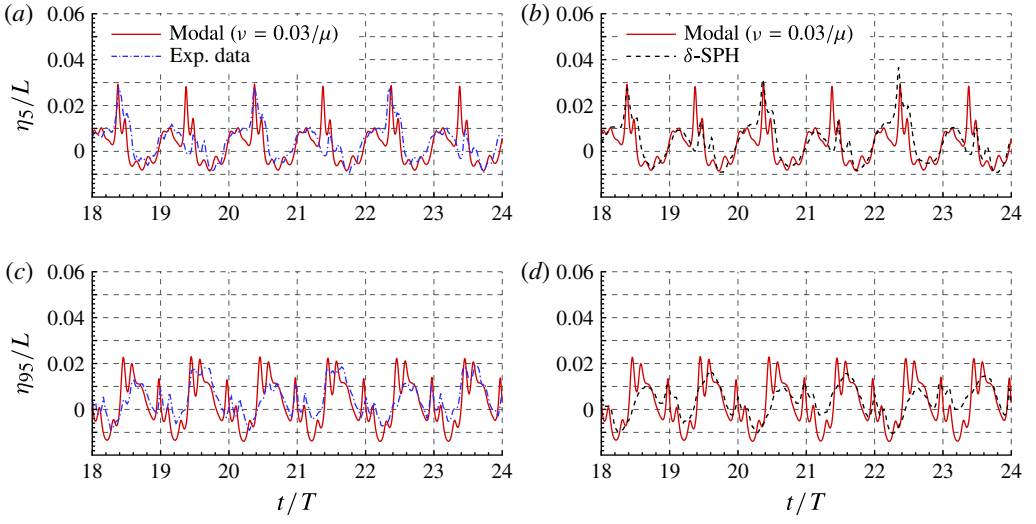


FIGURE 7. (Colour online) Series 3, $\sigma^* = 3.927$ s^{-1} ($\sigma^*/\sigma_r^* = 2.307$), and (*a*,*b*) $x^*/L^* = 0.05$, (*c*,*d*) $x^*/L^* = 0.95$.

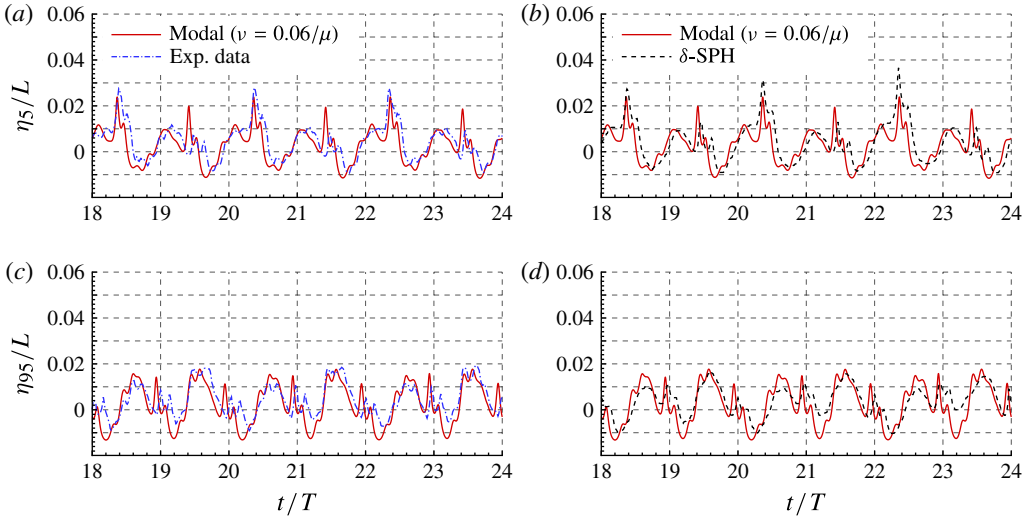


FIGURE 8. (Colour online) Series 3, $\sigma^* = 3.927$ s^{-1} ($\sigma^*/\sigma_r^* = 2.307$), and (*a*,*b*) $x^*/L^* = 0.05$, (*c*,*d*) $x^*/L^* = 0.95$.

the opposite wall, the experimental wavefront breaks and several splash-up cycles are generated (figure 12*c*). This phenomenon cannot be described by the numerical model, which, based on depth-averaged equations, tends to keep the front of the travelling bore more compact and localized. This leads to a delay of the numerical signal with respect to the experimental one (figure 11*c*,*d*). In any case, the wave-breaking process seems to be properly described, as shown by the large amount of vorticity generated by the numerical model (figure 12*c*). When the travelling bore reaches the opposite wall, the numerical and experimental free surfaces return to be in synchronization.

https://doi.org/10.1017/jfm.2014.127 Published online by Cambridge University Press

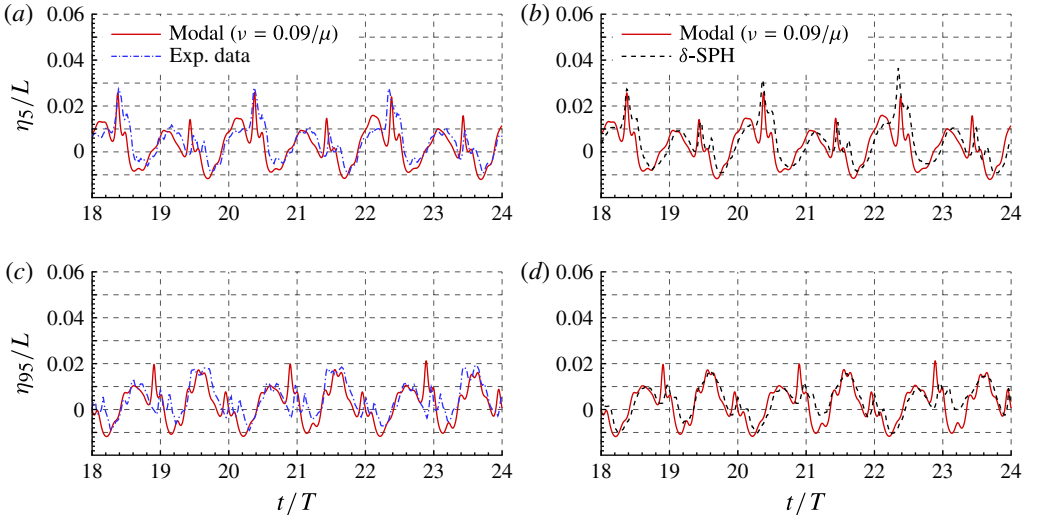


FIGURE 9. (Colour online) Series 3, $\sigma^* = 3.927$ s^{-1} ($\sigma^*/\sigma_r^* = 2.307$), and (*a*,*b*) $x^*/L^* = 0.05$, (*c*,*d*) $x^*/L^* = 0.95$.

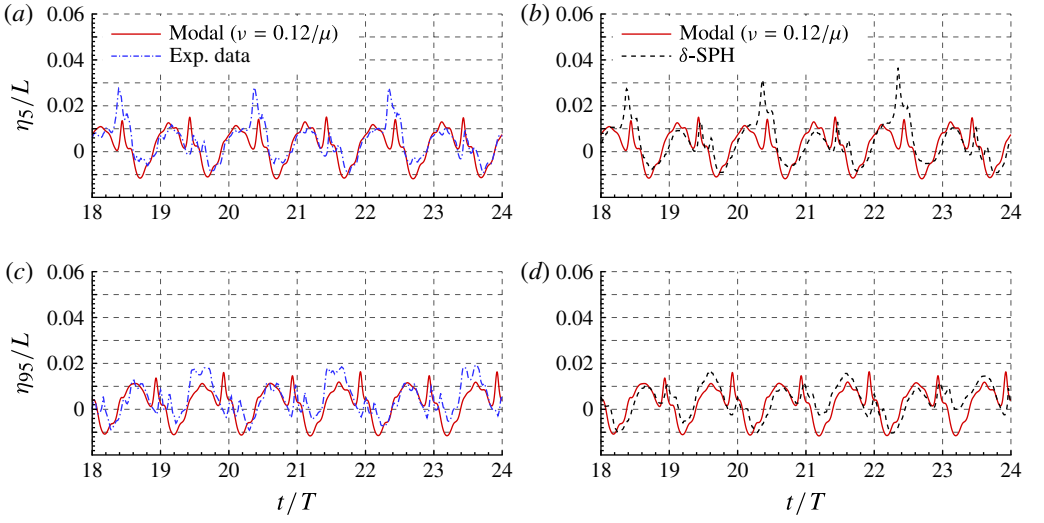


FIGURE 10. (Colour online) Series 3, $\sigma^* = 3.927$ s^{-1} ($\sigma^*/\sigma_r^* = 2.307$), and (*a*,*b*) $x^*/L^* = 0.05$, (*c*,*d*) $x^*/L^* = 0.95$.

The delay of the numerical results in comparison to the experimental data is, generally, not so evident from the signals recorded at fixed positions because of the large velocity of the wavefront but, nonetheless, is always present. This is, for example, what happens for the roll case described in figures 13 and 14 (Series R3 with $\sigma^*/\sigma_r^* = 1.1$). In this case the advance is rather small (figure 14*c*) and it is, practically, imperceptible in figure 13. In any case, the overall behaviour is the same as for the previous case and it is observable also in the cases that follow.

For $h_0^*/L^* = 0.069$, we considered a sway case with $\sigma^*/\sigma_r^* = 1.1$ (Series S2) and a roll case with $\sigma^*/\sigma_r^* = 1$ (Series R2). The comparisons with the experiments are

https://doi.org/10.1017/jfm.2014.127 Published online by Cambridge University Press

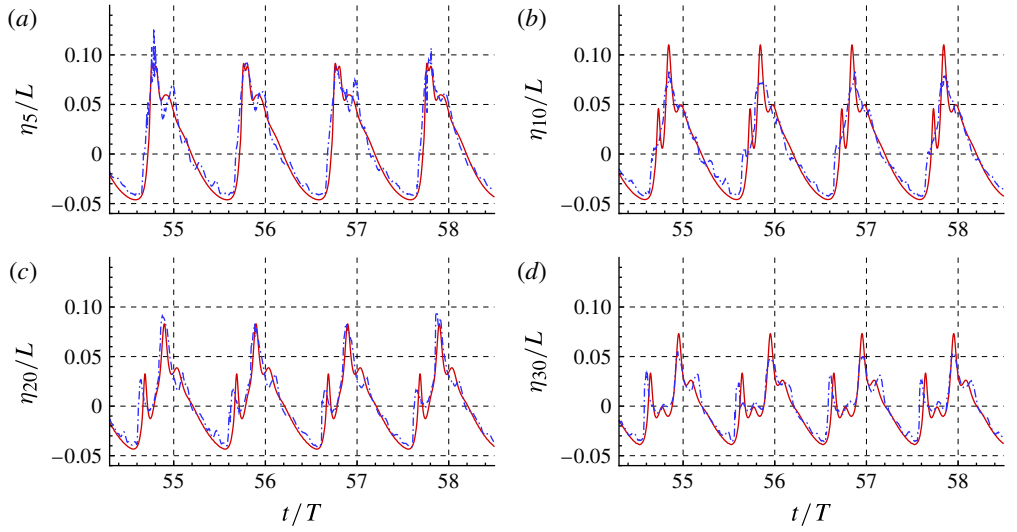


FIGURE 11. (Colour online) Series S3, $\sigma^* = 2.826\ \mathrm{s}^{-1}$ ($\sigma^*/\sigma_r^* = 0.95$). Comparison between the proposed model (solid line) and the experiments (dot-dashed line).

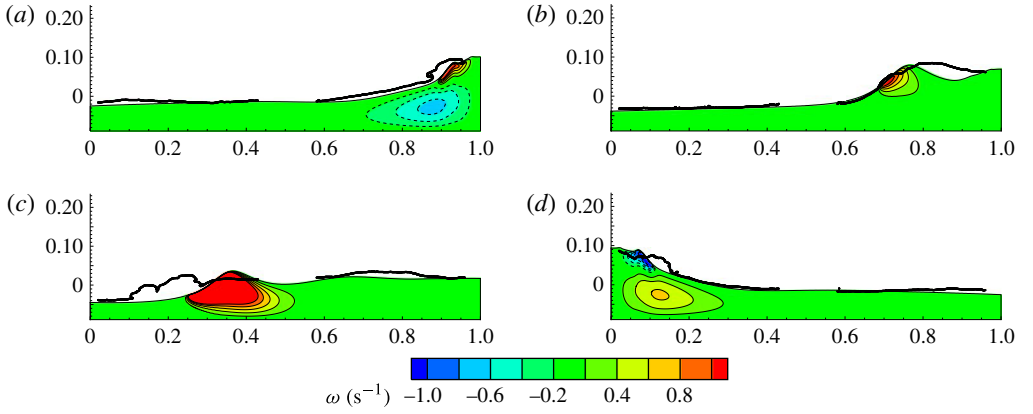


FIGURE 12. (Colour online) Series S3, $\sigma^* = 2.826\ \mathrm{s}^{-1}$ ($\sigma^*/\sigma_r^* = 0.95$). The contour lines of the vorticity field as predicted by the sloshing model (dashed lines for negative values, solid lines for positive values) and the free surface measured during the experiments (thick black solid lines) at different time instants.

shown in figures 15–18. The overall agreement is good even if for the roll case the experimental signals at fixed positions are disturbed by some spurious oscillations (see figure 17). These are probably due to a small swirling motion that is generated inside the tank. In any case this does not influence the overall behaviour of the experimental test. For Series S2 and R2 we selected some interesting snapshots of the free-surface evolution. Specifically, let us focus on figure 16(*d*) and figure 18(*d*). In both these panels a single free-surface bump evolves just after the run down at the sidewall of the tank. Similarly to the experiments, the proposed model remarkably predicts two breaking events: one due to the breaking front of the travelling wave and the other one caused by the wave run down at the wall. Although the second breaking event

https://doi.org/10.1017/jfm.2014.127 Published online by Cambridge University Press

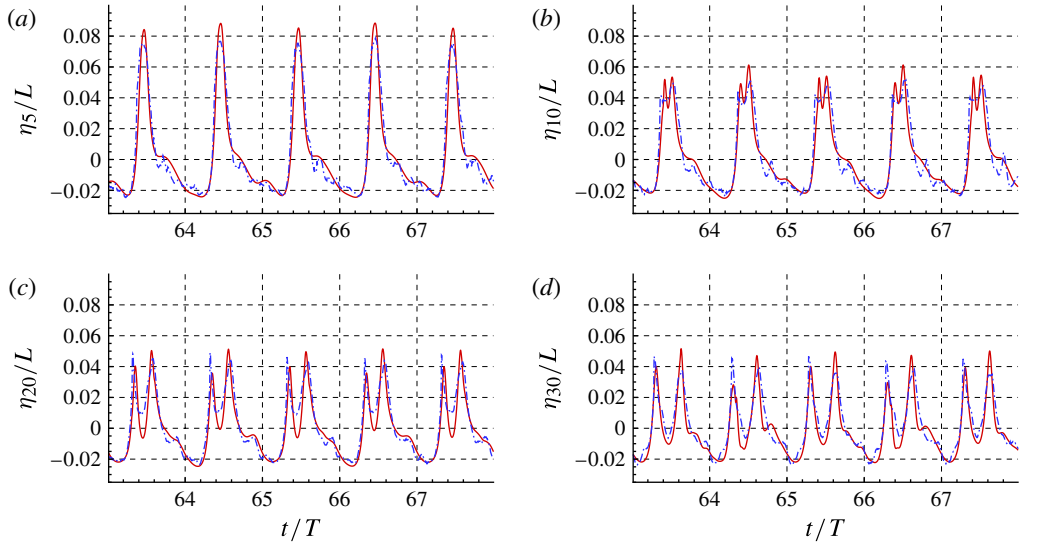


FIGURE 13. (Colour online) Series R3, $\sigma^* = 3.272$ s^{-1} ($\sigma^*/\sigma_r^* = 1.1$). Comparison between the proposed model (solid line) and the experiments (dot-dashed line).

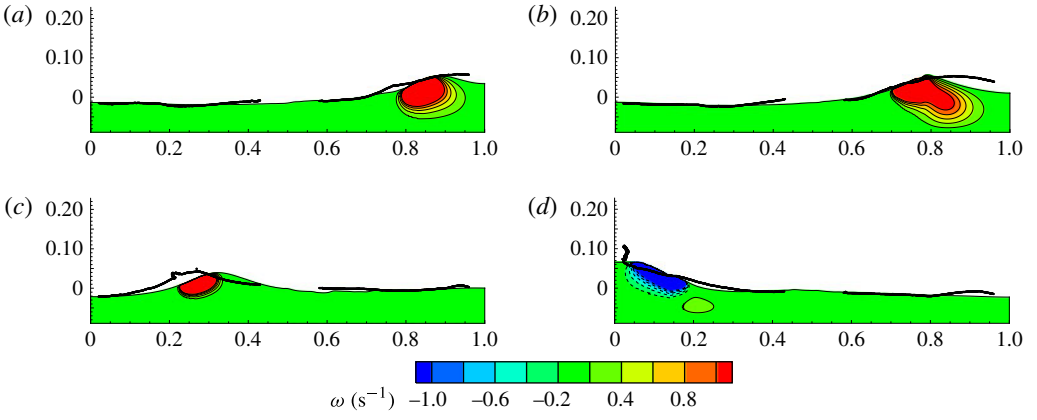


FIGURE 14. (Colour online) Series R3, $\sigma^* = 3.272$ s^{-1} ($\sigma^*/\sigma_r^* = 1.1$). The contour lines of the vorticity field as predicted by the sloshing model (dashed lines for negative values, solid lines for positive values) and the free surface measured during the experiments (thick black solid lines) at different time instants.

is only roughly described (the experiments show a strong and persistent vortex close to the bottom corner of the tank), this is sufficient to provide a fair approximation of the wave-breaking dissipation.

The last part of the present analysis is devoted to the cases characterized by very shallow depths, that is, Series S1 and R1 ($h_0^*/L^* = 0.034$). Both these cases display some analogies and a similar evolution. The free-surface time histories are shown in figures 19 and 21. In comparison to the experimental measurements, the numerical signals are characterized by several oscillations even if the overall behaviour is represented fairly well (see also figures 20 and 22). Similarly to the sway case

https://doi.org/10.1017/jfm.2014.127 Published online by Cambridge University Press

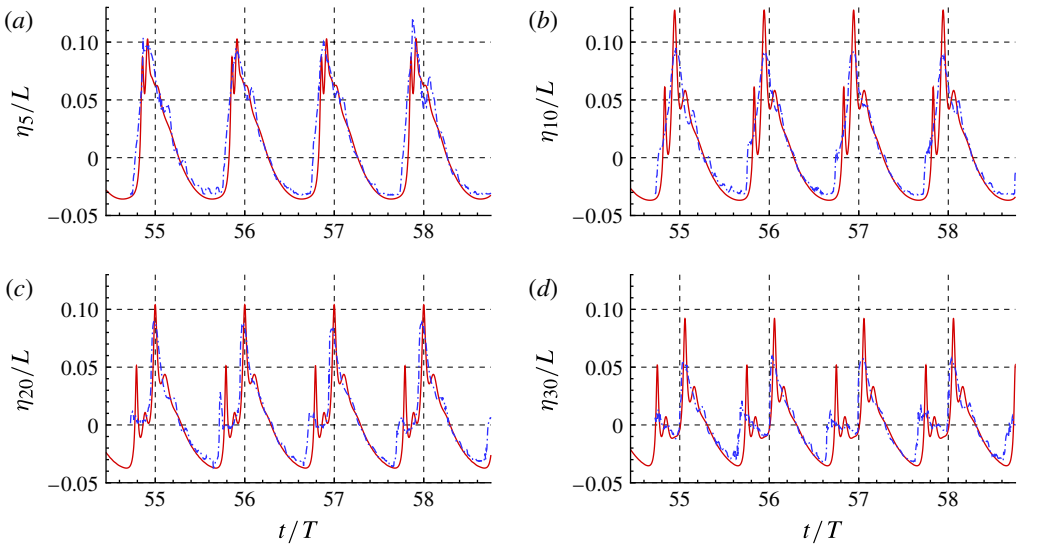


FIGURE 15. (Colour online) Series S2, $\sigma^* = 2.866$ s^{-1} ($\sigma^*/\sigma_r^* = 1.1$). Comparison between the proposed model (solid line) and the experiments (dot-dashed line).

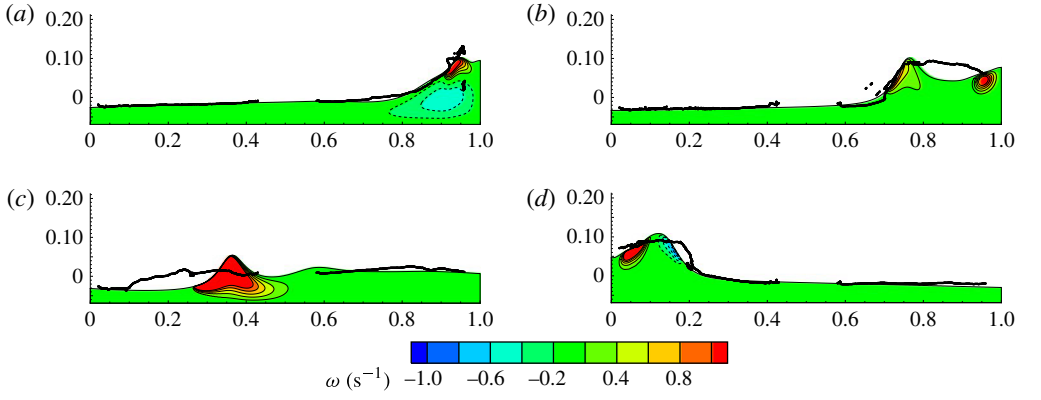


FIGURE 16. (Colour online) Series S2, $\sigma^* = 2.866$ s^{-1} ($\sigma^*/\sigma_r^* = 1.1$). The contour lines of the vorticity field as predicted by the sloshing model (dashed lines for negative values, solid lines for positive values) and the free surface measured during the experiments (thick black solid lines) at different time instants.

described in figure 6, these oscillations, typical of undular bores, are probably due to an underestimation of the wave-breaking dissipation. The excess of energy excites the dispersive mechanisms described by the model and leads to the generation of undular-type wave trains. Such a phenomenon highlights some possible limits of the proposed model in describing breaking events in very shallow water. This issue is addressed in the following section.

3.3.1. *Limits of applicability*

As a final part of the present work, we inspect the limits of applicability of the proposed model. A preliminary condition that must be satisfied for the consistency of

https://doi.org/10.1017/jfm.2014.127 Published online by Cambridge University Press

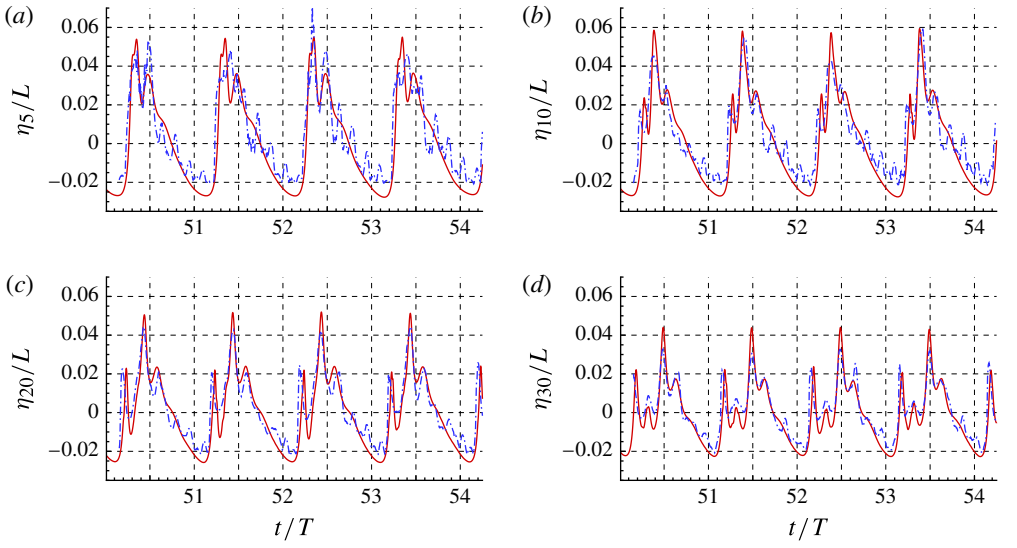


FIGURE 17. (Colour online) Series R2, $\sigma^* = 2.605$ s^{-1} ($\sigma^*/\sigma_r^* = 1$). Comparison between the proposed model (solid line) and the experiments (dot-dashed line).

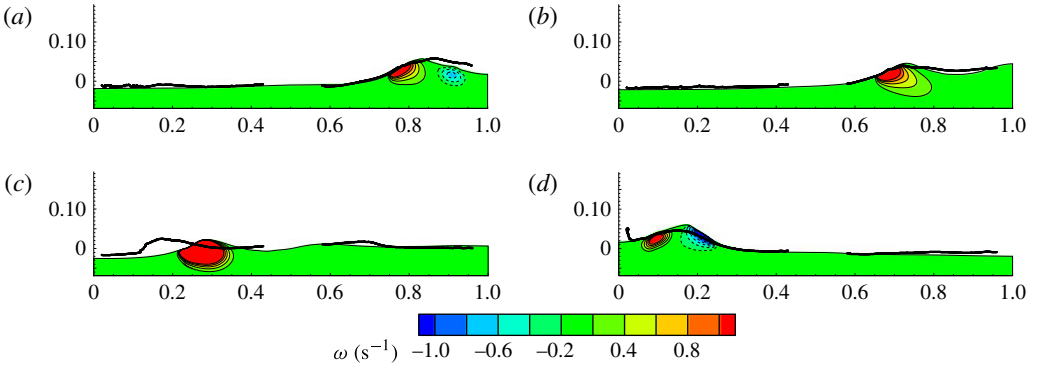


FIGURE 18. (Colour online) Series R2, $\sigma^* = 2.605$ s^{-1} ($\sigma^*/\sigma_r^* = 1$). The contour lines of the vorticity field as predicted by the sloshing model (dashed lines for negative values, solid lines for positive values) and the free surface measured during the experiments (thick black solid lines) at different time instants.

the scheme is $F_1/\mu = O(1)$. For the roll motion we assume that $(x_C - x_0)$, $(z_C - z_0)$ and w_C are of order one. Since the axis of rotation has been placed in the middle of the tank bottom and the angle of rotation is small, the above conditions are largely satisfied in all the roll cases shown in the present work. Assuming that the motion of the centre of mass is weak, we can approximate $(x_C - x_0)$ and $(z_C - z_0)$ by using the coordinates of the centre of mass in still-water conditions. We denote these approximated terms by ℓ_1 and ℓ_2, respectively. Under these assumptions, $F_1/\mu = O(1)$ may be reduced to the following bounds:

$$\frac{\sin\theta}{\mu} = O(1), \quad \frac{a_{0,1}}{\mu} = O(1), \quad a_{0,2} = O(1), \quad \mu\ddot{\theta}\ell_2 = O(1),$$

https://doi.org/10.1017/jfm.2014.127 Published online by Cambridge University Press

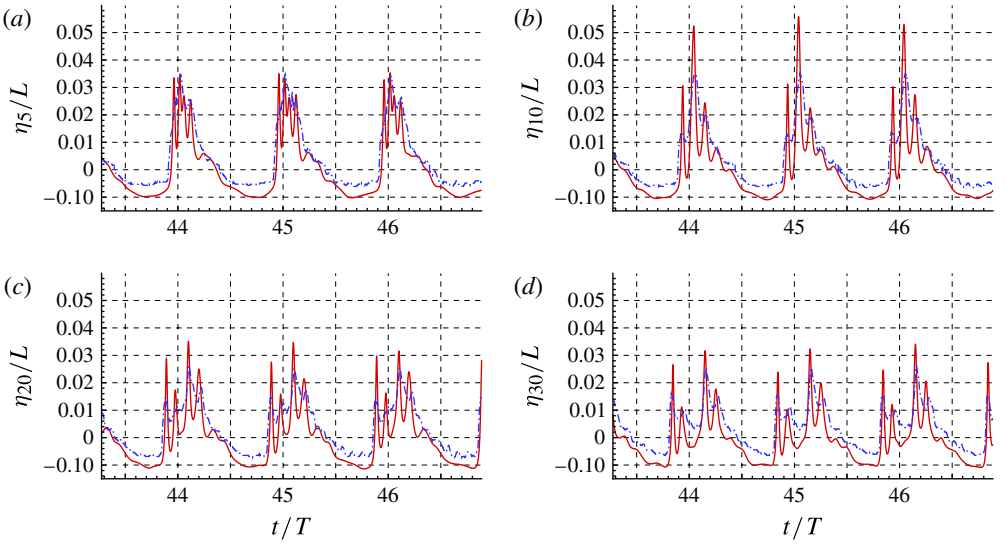


FIGURE 19. (Colour online) Series S1, $\sigma^* = 2.272$ s^{-1} ($\sigma^*/\sigma_r^* = 1.25$). Comparison between the proposed model (solid line) and the experiments (dot-dashed line).

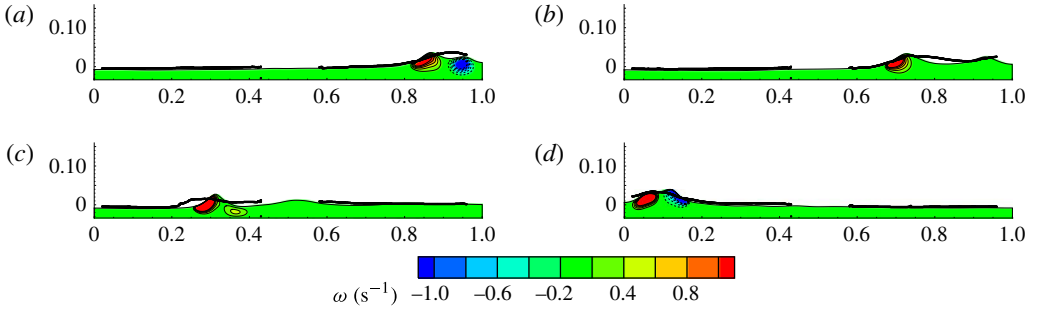


FIGURE 20. (Colour online) Series S1, $\sigma^* = 2.272$ s^{-1} ($\sigma^*/\sigma_r^* = 1.25$). The contour lines of the vorticity field as predicted by the sloshing model (dashed lines for negative values, solid lines for positive values) and the free surface measured during the experiments (thick black solid lines) at different time instants.

$$\dot{\theta}^2 \ell_1 = O(1), \quad \mu \dot{\theta} w_C = O(1). \tag{3.5a,b,c,d,e,f}$$

Since we have assumed that $\ell_1, w_C = O(1)$ and $\mu \ll 1$, the fifth condition ensures the fulfilment of the last one (which is neglected hereinafter). Further, we drop the bound on $a_{0,2}$, since the verticalacceleration is not considered in the present analysis. The remaining terms are evaluated by using the dimensionless forms of the expressions in (3.2*a*,*b*), that is

$$x(t) = A \sin(\sigma t), \quad \theta(t) = \theta_0 \sin(\sigma t). \tag{3.6a,b}$$

We obtain the following conditions:

$$\frac{\theta_0}{\mu} = O(1), \quad \frac{A\sigma^2}{\mu} = O(1), \quad \mu \theta_0 \sigma^2 \ell_2 = O(1), \quad \theta_0^2 \sigma^2 \ell_1 = O(1). \tag{3.7a,b,c,d}$$

https://doi.org/10.1017/jfm.2014.127 Published online by Cambridge University Press

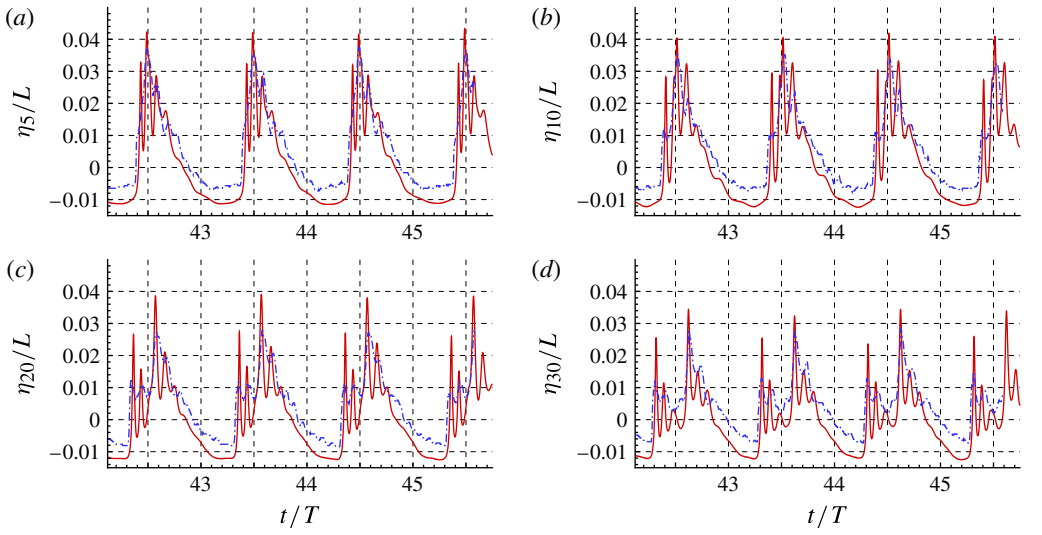


FIGURE 21. (Colour online) Series R1, $\sigma^* = 2.181$ s^{-1} ($\sigma^*/\sigma_r^* = 1.2$). Comparison between the proposed model (solid line) and the experiments (dot-dashed line).

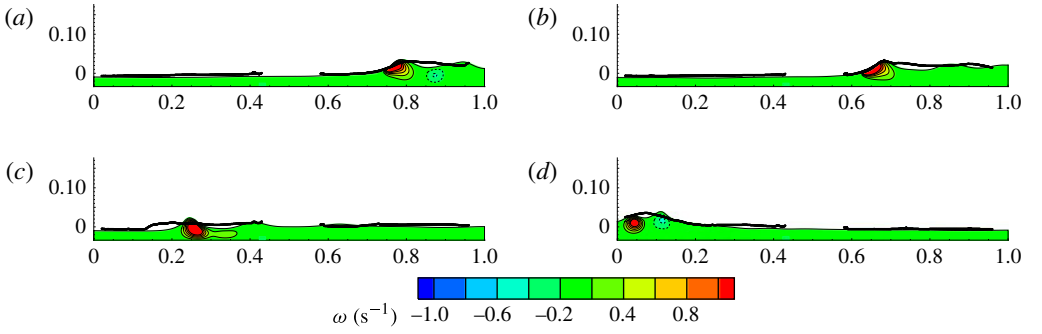


FIGURE 22. (Colour online) Series R1, $\sigma^* = 2.181$ s^{-1} ($\sigma^*/\sigma_r^* = 1.2$). The contour lines of the vorticity field as predicted by the sloshing model (dashed lines for negative values, solid lines for positive values) and the free surface measured during the experiments (thick black solid lines) at different time instants.

In the roll cases shown in the present work, $\ell_2 = h/2$ while $\ell_1 = 0$ and, therefore, the last bound can be neglected. In dimensional variables, the remaining conditions are equivalent to the following requirements:

$$\gamma_1 = \frac{\theta_0}{\mu} = O(1), \quad \gamma_2 = \frac{A^*(\sigma^*)^2}{\mu^2 g^*} = O(1), \quad \gamma_3 = \frac{\theta_0(\sigma^*)^2 \ell_2^*}{\mu g^*} = O(1). \quad (3.8a,b,c)$$

It is understood that the above conditions are valid for a circular frequency below the bifurcation frequency, that is, for $\sigma^* \leqslant \sigma_b^*$. The values of γ_1, γ_2 and γ_3 for the sloshing cases described up to here are summarized in table 4. In all cases the third condition is largely satisfied, since its values range from 10^{-3} to 10^{-2} (note that θ_0 is expressed in radians). The condition on γ_1 is always fulfilled as well, even though it somehow seems too elusive, since spurious oscillations may already arise for $\gamma_1 \geqslant 1/2$. For γ_2,

https://doi.org/10.1017/jfm.2014.127 Published online by Cambridge University Press

Sway and roll	σ^* (s^{-1})	γ_1	γ_2	γ_3	ϵ_5	ϵ_{30}
Series 1	2.856	—	6.93	—	1.08	—
Series 2	3.393	—	7.51	—	2.40	—
Series 3	2.094	—	34.76	—	2.00	—
Series S1	2.272	—	15.48	—	1.32	0.88
Series S2	2.866	—	12.13	—	1.66	1.09
Series S3	2.826	—	5.49	—	1.68	1.12
Series R1	2.181	0.513	—	0.0085	1.32	0.97
Series R2	2.605	0.253	—	0.0121	1.08	0.72
Series R3	3.272	0.196	—	0.0190	1.12	0.79

TABLE 4. The values of the parameters γ_1, γ_2 and γ_3 defined in (3.8*a*,*b*,*c*). The parameters ϵ_5 and ϵ_{30} have been computed by using the free-surface signals at $x^*/L^* = 0.05$ and $x^*/L^* = 0.3$ (that is, η^*_5 and η^*_{30}).

the proposed model proved to work properly up to $\gamma_2 \simeq 10$, that is, a bit beyond the bound in (3.8*a*,*b*,*c*). For larger values, the numerical results are affected by spurious oscillations whose intensity increases as γ_2 becomes larger and larger. Consistently, the worst case is that of Series 3 with $\sigma^* = 2.094$ s^{-1} (figure 6) where $\gamma_2 = 35$.

Further conditions that have to be satisfied are $\epsilon\mu^2 \ll 1$ and $\mu^4 \ll 1$. For sloshing motions the dispersive parameter μ depends only on the tank geometry (while, for example, in the case of coastal flows it depends on the wavelength). This implies that, if the tank dimensions ensure $\mu^2 \ll 1$, the proposed model can properly describe sloshing cases with $\epsilon = O(1)$, that is, highly nonlinear phenomena. This is clearly shown in the last column of table 4, where the value of ϵ has been computed by using the free-surface signals at $x^*/L^* = 0.05$ and $x^*/L^* = 0.3$ (that is, η^*_5 and η^*_{30}).

4. Conclusions

Following the approach described in Antuono & Brocchini (2013), the sloshing model proposed in Antuono *et al.* (2012) for rectangular tanks in shallow-water conditions has been extended to include wave-breaking processes. The vorticity field has been obtained by solving the linearized equation of the vorticity with free-surface boundary conditions that have been derived from the criteria typical of near-shore circulation models and described in Veeramony & Svendsen (2000). In agreement with the majority of depth-averaged models, the turbulent terms have been modelled through a Boussinesq closure while the turbulent viscosity has been assumed to be constant all over the liquid domain. The intensity of the turbulent viscosity has been calibrated by using the experimental campaign described in Bouscasse *et al.* (2013), while a second experimental campaign has been specifically conceived to validate the model.

Both sway and roll motions have been analysed, as well as different filling depths and moderate to strong breaking events (from bores to plunging breaking waves). In all cases the model proved to be robust and reliable in the prediction of the sloshing phenomena and to be effective in a wider range of filling depths and excitation amplitudes than other existing shallow-water sloshing models (see e.g. Faltinsen & Timokha 2002; Hill 2003; Antuono *et al.* 2012).

Some spurious oscillations, probably caused by an underestimation of the wave-breaking dissipation, have been observed for very shallow depths and large excitations.

https://doi.org/10.1017/jfm.2014.127 Published online by Cambridge University Press

This suggests that some care has to be used when dealing with this kind of configuration. Specifically, we observed that the proposed model applies better to sway cases characterized by $\gamma_2 < 10$ and to roll motion with $\gamma_1 < 1/2$.

Apart from these limits, the proposed scheme may be regarded as a valuable tool for the prediction of sloshing phenomena in shallow-water conditions. In general, sloshing flows involve rather complex phenomena, including breaking wave, multiphase flows, splash-up and so on, which are extremely difficult to reproduce numerically. Numerical models based on the solution of the Navier–Stokes equations, although theoretically able to reproduce these phenomena, are extremely time-consuming. Further, they often show some difficulties for long-time simulations (e.g. problems in satisfying mass and energy conservation due to numerical dissipation).

In this context, the construction of an efficient numerical model for shallow-water condition, like the proposed one, is very useful. First, its coupling with potential flow methods for ship motion predictions can be useful to estimate the mutual interaction between ship motions and the sloshing flows in internal tanks. Second, the capability to capture the occurrence of wave breaking in the tank can be useful to estimate the occurrence of strong local impact loads on the tank wall, eventually triggering hydroelastic effects.

Acknowledgements

This research activity is partially funded by the Research Council of Norway through the Centres of Excellence funding scheme AMOS, project number 223254, and within the Research Project 'Numerical Simulation of Complex System'. It has been also supported by the Flagship Project RITMARE, The Italian Research for the Sea, coordinated by the Italian National Research Council and funded by the Italian Ministry of Education, University and Research within the National Research Program 2011–2013.

The authors would like to thank Dr Andrea Colagrossi and Dr Benjamin Bouscasse for the SPH simulations shown in this work.

Appendix A. Derivation of the sloshing model

Let us consider the one-dimensional semi-integrated model proposed in Antuono & Brocchini (2013). The velocity field is decomposed into a depth-averaged component and a deviation, that is, $u = U + \delta u$, where

$$u(t, x, z) = U(t, x) + \delta u(t, x, z) \quad \text{with } U(t, x) = \frac{1}{d}\int_{-h}^{\epsilon\eta} u(t, x, z)\,\mathrm{d}z. \tag{A 1}$$

The deviation is given by

$$\delta u = -\mu^2 \left[\int_z^{\epsilon\eta} w_x\,\mathrm{d}\zeta - \frac{1}{d}\int_{-h}^{\epsilon\eta}\mathrm{d}z\int_z^{\epsilon\eta} w_x\,\mathrm{d}\zeta\right] + R, \tag{A 2}$$

where

$$R = -\int_z^{\epsilon\eta}\omega\,\mathrm{d}\zeta + \frac{1}{d}\int_{-h}^{\epsilon\eta}\mathrm{d}z\int_z^{\epsilon\eta}\omega\,\mathrm{d}\zeta \tag{A 3}$$

and ω is the vorticity field (horizontal component only). This variable is assumed to be known and is modelled similarly to the work of Veeramony & Svendsen

https://doi.org/10.1017/jfm.2014.127 Published online by Cambridge University Press

(2000). Neglecting the turbulent stresses at the free surface and at the bottom, the one-dimensional semi-integrated model reads

$$\begin{cases} \eta_t + (Ud)_x = 0, \\ U_t + \epsilon U U_x + \eta_x + \dfrac{\mu^2}{d}\displaystyle\int_{-h}^{\epsilon\eta} \Upsilon_{xt}\,\mathrm{d}z + \dfrac{\epsilon\mu^2}{d}\int_{-h}^{\epsilon\eta} M_x^{(z)}\,\mathrm{d}z \\ \quad + \epsilon\dfrac{M^{(x)}}{d} + \dfrac{\mu^2}{d}\displaystyle\int_{-h}^{\epsilon\eta} T_x^{(z)}\,\mathrm{d}z + \mu^2\dfrac{T^{(x)}}{d} = 0, \end{cases} \tag{A 4}$$

where

$$\Upsilon = \int_z^{\epsilon\eta} w\,\mathrm{d}\zeta, \quad M^{(x)} = \left[\int_{-h}^{\epsilon\eta} \delta u^2\,\mathrm{d}z\right]_x, \quad T^{(x)} = \left[\int_{-h}^{\epsilon\eta} \langle\hat{u}^2\rangle\,\mathrm{d}z\right]_x, \tag{A5a,b,c}$$

$$M^{(z)} = \left[\int_z^{\epsilon\eta} uw\,\mathrm{d}\zeta\right]_x - w^2, \quad T^{(z)} = \left[\int_z^{\epsilon\eta} \langle\hat{u}\hat{w}\rangle\,\mathrm{d}\zeta\right]_x - \langle\hat{w}^2\rangle. \tag{A6a,b}$$

A Boussinesq closure is adopted to estimate the turbulent terms:

$$\langle\hat{u}^2\rangle = -2\nu_T u_x, \quad \langle\hat{w}^2\rangle = -2\nu_T w_z, \quad \langle\hat{u}\hat{w}\rangle = -\nu_T(u_z + \mu^2 w_x). \tag{A7a,b,c}$$

Hereinafter, we neglect all terms that give contributions of order $O(\epsilon\mu^2, \mu^4)$ inside system (A 4). First, we derive an approximate expression for the vertical velocity w.

The continuity equation and (A 2) for δu give

$$w_z = -U_x - \delta u_x = -U_x - R_x + O(\mu^2), \tag{A 8}$$

while the boundary condition at the free surface is $w|_{\epsilon\eta} = \eta_t + O(\epsilon, \epsilon\mu^2)$. Then, integrating over the depth, we obtain

$$w = \eta_t + U_x(\epsilon\eta - z) + \int_z^{\epsilon\eta} R_x\,\mathrm{d}\zeta + O(\epsilon, \mu^2). \tag{A 9}$$

Using the above expression and $\eta_t = -hU_x + O(\epsilon)$ (the continuity equation of the system (A 4)), we find

$$\Upsilon = -hU_x(\epsilon\eta - z) + U_x\frac{(\epsilon\eta - z)^2}{2} + \int_z^{\epsilon\eta}\mathrm{d}\zeta\int_\zeta^{\epsilon\eta} R_x\,\mathrm{d}\xi + O(\epsilon, \mu^2), \tag{A 10}$$

$$\frac{\mu^2}{d}\int_{-h}^{\epsilon\eta}\Upsilon_{xt}\,\mathrm{d}z = -\frac{\mu^2 h^2}{3}U_{xxt} + \frac{\mu^2}{h}\int_{-h}^{\epsilon\eta}\mathrm{d}z\int_z^{\epsilon\eta}\mathrm{d}\zeta\int_\zeta^{\epsilon\eta} R_{xxt}\,\mathrm{d}\xi + O(\epsilon\mu^2, \mu^4). \tag{A 11}$$

Similarly, we obtain

$$\frac{\epsilon}{d}M^{(x)} = \frac{\epsilon}{d}\left[\int_{-h}^{\epsilon\eta} R^2\,\mathrm{d}z\right]_x + O(\epsilon\mu^2), \tag{A 12}$$

$$\frac{\mu^2}{d}T^{(x)} = -2\nu_T\mu^2 U_{xx} - 2\nu_T\frac{\mu^2}{h}\int_{-h}^{\epsilon\eta} R_{xx}\,\mathrm{d}z + O(\epsilon\mu^2, \mu^4). \tag{A 13}$$

https://doi.org/10.1017/jfm.2014.127 Published online by Cambridge University Press

For the last turbulent term, we first simplify the turbulent stresses as follows:

$$\langle \hat{w}^2 \rangle = 2\nu_T u_x = 2\nu_T U_x + 2\nu_T R_x + O(\mu^2), \quad \langle \hat{u}\hat{w} \rangle = -\nu_T \omega + O(\mu^2). \tag{A14a,b}$$

Then, we obtain

$$\frac{\mu^2}{d}\int_{-h}^{\epsilon\eta} T_x^{(z)}\,\mathrm{d}z = -\nu_T \frac{\mu^2}{h}\int_{-h}^{\epsilon\eta}\left[\int_z^{\epsilon\eta}\omega\,\mathrm{d}\zeta\right]_{xx}\mathrm{d}z - 2\nu_T\mu^2 U_{xx} - 2\nu_T\frac{\mu^2}{h}\int_{-h}^{\epsilon\eta} R_{xx}\,\mathrm{d}z + O(\epsilon\mu^2, \mu^4). \tag{A 15}$$

A.1. *Details of the computation*

Using the summation in (2.8), we find

$$\int_z^{\epsilon\eta}\omega\,\mathrm{d}\zeta = d\sum_{n\in\mathbb{Z}}\frac{\mathrm{e}^{\mathrm{i}n\pi x}}{2\mathrm{i}}\sum_{m=1}^{+\infty}\frac{\phi_{n,m}(t)}{m\pi}[-1+\cos(m\pi y)], \tag{A 16}$$

$$R = -d\sum_{n\in\mathbb{Z}}\frac{\mathrm{e}^{\mathrm{i}n\pi x}}{2\mathrm{i}}\sum_{m=1}^{+\infty}\frac{\phi_{n,m}(t)}{m\pi}\cos(m\pi y). \tag{A 17}$$

Then, it follows that

$$\int_{-h}^{\epsilon\eta} R_{xx}\,\mathrm{d}z = O(\epsilon), \tag{A 18}$$

$$\int_{-h}^{\epsilon\eta}\left[\int_z^{\epsilon\eta}\omega\,\mathrm{d}\zeta\right]_{xx}\mathrm{d}z = h^2\sum_{n\in\mathbb{Z}}(n\pi)^2\frac{\mathrm{e}^{\mathrm{i}n\pi x}}{2\mathrm{i}}\sum_{m=1}^{+\infty}\frac{\phi_{n,m}(t)}{m\pi} + O(\epsilon), \tag{A 19}$$

$$\int_{-h}^{\epsilon\eta}\mathrm{d}z\int_z^{\epsilon\eta}\mathrm{d}\zeta\int_\zeta^{\epsilon\eta} R_{xxt}\,\mathrm{d}\xi = h^4\sum_{n\in\mathbb{Z}}(n\pi)^2\frac{\mathrm{e}^{\mathrm{i}n\pi x}}{2\mathrm{i}}\sum_{m=1}^{+\infty}\frac{\dot{\phi}_{n,m}(t)}{(m\pi)^3} + O(\epsilon). \tag{A 20}$$

For the nonlinear term, we obtain

$$R^2 = -\frac{d^2}{4}\sum_{p,q\in\mathbb{Z}}\mathrm{e}^{\mathrm{i}(p+q)\pi x}\sum_{r,s=1}^{+\infty}\frac{\phi_{p,r}(t)}{r\pi}\frac{\phi_{q,s}(t)}{s\pi}\cos(r\pi y)\cos(s\pi y), \tag{A 21}$$

and, integrating, we find that

$$\int_{-h}^{\epsilon\eta} R^2\,\mathrm{d}z = -\frac{d^3}{8}\sum_{p,q\in\mathbb{Z}}\mathrm{e}^{\mathrm{i}(p+q)\pi x}\sum_{m=1}^{+\infty}\frac{\phi_{p,m}(t)\phi_{q,m}(t)}{(m\pi)^2}. \tag{A 22}$$

Then, it follows that

$$\frac{1}{d}\left[\int_{-h}^{\epsilon\eta} R^2\,\mathrm{d}z\right]_x = h^2\sum_{p,q\in\mathbb{Z}}(p+q)\pi\frac{\mathrm{e}^{\mathrm{i}(p+q)\pi x}}{8\mathrm{i}}\sum_{m=1}^{+\infty}\frac{\phi_{p,m}(t)\phi_{q,m}(t)}{(m\pi)^2} + O(\epsilon). \tag{A 23}$$

For the sake of simplicity, the above term may be rearranged as follows:

$$\frac{1}{d}\left[\int_{-h}^{\epsilon\eta} R^2\,\mathrm{d}z\right]_x = h^2\sum_{n\in\mathbb{Z}}(n\pi)\frac{\mathrm{e}^{\mathrm{i}n\pi x}}{8\mathrm{i}}\sum_{p\in\mathbb{Z}}\sum_{m=1}^{+\infty}\frac{\phi_{p,m}(t)\phi_{n-p,m}(t)}{(m\pi)^2} + O(\epsilon). \tag{A 24}$$

https://doi.org/10.1017/jfm.2014.127 Published online by Cambridge University Press

A.2. *Breaking criterion and boundary conditions*

In Veeramony & Svendsen (2000), the inception of breaking for the weakly nonlinear model was placed at the wave location where the free-surface slope exceeded 20°, that is, where $|\eta^*_{x^*}| \geqslant \tan(\pi/9)$. We follow this criterion, but add a further condition to be fulfilled for breaking to occur. Specifically, we also require $(u^*\eta^*_{x^*}) \leqslant -0.05\sqrt{g^* h^*_0}$. This ensures that breaking occurs in the same direction as wave propagation and avoids unphysical breaking events associated with the wave trains that are generated in sloshing motions. As a preliminary check on the proposed breaking criterion, we simulated the same sloshing cases as considered in Antuono *et al.* (2011). Indeed, since these are characterized by non-breaking waves, the numerical simulations should coincide with those shown in Antuono *et al.* (2011). In all cases we did not observe any difference, thus confirming the reliability of the breaking criterion.

The breaking point is, generally, at the toe of a steep wave. In Veeramony & Svendsen's model, the interval of wave breaking grows during the evolution and, finally, extends from the breaking point up to the first peak of the wave. The time scaling of its evolution is related to the wave period. Since this approach is unnecessarily too complex for the sloshing model at hand, we simplify it as follows. We neglect the growth of the breaking interval during evolution and assume that it immediately extends from the breaking point up to the roller end point. Specifically, the end point is set where the free-surface slope is smaller than 5°, that is, $|\eta^*_{x^*}| \leqslant \tan(\pi/36)$. The breaking point and the roller end point are updated during the evolution of sloshing.

In Veeramony & Svendsen's (2000) model, the boundary conditions for the vorticity are assigned along the lower boundary of the 'wave roller' η_e (generally different from the free surface) in the spatial interval over which breaking occurs. We simplify this approach and make the assignment directly along the actual free surface, that is, η.

Let us denote by x^*_{ini} and x^*_{end} the initial and end points of the breaking region and, for the sake of simplicity, let us assume that $x^*_{ini} < x^*_{end}$. Then, according to Veeramony & Svendsen, the boundary datum for the vorticity is

$$\omega_f = \begin{cases} 15.75 W_0 [1 - \mathrm{e}^{-40(x^* - x^*_{ini})/\ell^*}][1 - (x^* - x^*_{ini})/\ell^*], & x^* \in [x^*_{ini}, x^*_{end}], \\ 0, & \text{elsewhere}, \end{cases} \tag{A 25}$$

where $\ell^* = (x^*_{end} - x^*_{ini})$ and W_0 is a factor that derives from the representation of Veeramony & Svendsen's results into our scaling. Specifically,

$$W_0 = \frac{U^*_1 h^*_1}{\omega^*_0 (h^*_2)^2}, \tag{A 26}$$

where h^*_1 and U^*_1 are the depth and velocity measured at x^*_{ini}, and h^*_2 is the depth at x_{end^*}.

A.2.1. *Detection of x^*_{ini} and x^*_{end}*

The detection of x^*_{ini} and x^*_{end} by directly using $\eta^*_{x^*}$ is not reliable. Indeed, $\eta^*_{x^*}$ generally presents oscillations, which may lead to the detection of spurious breaking events. These, in turn, may induce further oscillations, leading to a feedback mechanism that makes the computation unstable.

For this reason (and exclusively for the detection of x^*_{ini} and x^*_{end}), a suitable filter is used to smooth $\eta^*_{x^*}$. Specifically, we define

$$\langle \eta^*_{x^*} \rangle = \frac{1}{\lambda^*} \int_{x^* - \lambda^*/2}^{x^* + \lambda^*/2} \eta^*_{s^*} \, \mathrm{d}s^*. \tag{A 27}$$

https://doi.org/10.1017/jfm.2014.127 Published online by Cambridge University Press

Using (2.5), it is easy to show that

$$\begin{aligned}\langle \eta^*_{x^*} \rangle &= -\sum_n nk^* H^*_n \sin(nk^* x^*) \left[\frac{2}{nk^* \lambda^*} \sin\left(\frac{nk^* \lambda^*}{2} \right) \right] \\ &= -\sum_n \frac{2H^*_n}{\lambda^*} \sin(nk^* x^*) \sin\left(\frac{nk^* \lambda^*}{2} \right), \end{aligned} \tag{A 28}$$

where $k^* = \pi/L^*$ is the wavenumber. The first expression in (A 28) highlights how the smoothing procedure modifies the original expression of $\eta^*_{x^*}$. The terms obtained through the smoothing decrease like $1/n$ and ensure a smaller content of high-order frequencies in the smoothed signal. The final expression in (A 28) suggests what the order of magnitude of λ^* should be. Specifically, we require that the smoothing procedure does not change its characteristics by varying the tank dimensions or the filling depth. Since we only have two spatial lengths, the only possible choices for λ^* are $\lambda^* = \alpha L^*$ or $\lambda^* = \beta h^*$, where α and β are dimensionless parameters. Using the adopted scaling, we find

$$\eta^*_{x^*} = -\epsilon\mu \sum_n n\pi H_n \sin(n\pi x), \tag{A 29}$$

$$\lambda^* = \alpha L^* \quad \Rightarrow \quad \langle \eta^*_{x^*} \rangle = -\epsilon\mu \sum_n 2\frac{H_n}{\alpha} \sin(n\pi x) \sin\left(n\frac{\pi}{2}\alpha \right), \tag{A 30}$$

$$\lambda^* = \beta h^* \quad \Rightarrow \quad \langle \eta^*_{x^*} \rangle = -\epsilon \sum_n 2\frac{H_n}{\beta} \sin(n\pi x) \sin\left(n\frac{\pi}{2}\beta\mu \right). \tag{A 31}$$

It is evident from the above expansions that the smoothing in the final expression changes its intensity over the modes because of the inner dependence on μ. On the contrary, in the expansion obtained by setting $\lambda^* = \alpha L^*$, the parameter μ appears as a magnitude parameter. This is consistent with the expansion for the original signal, $\eta^*_{x^*}$. As a consequence, in all the simulations shown in the present work, we use $\lambda^* = \alpha L^*$. Since the smoothing length has to be consistent with the shallow-water approximation, we also require $\alpha \ll 1$. Specifically, we found that $\alpha = 0.1$ is a good and reliable choice. In fact, a larger value would lead to a damping of the original signal, while a smaller value would not eliminate the high-frequency oscillations in $\eta^*_{x^*}$, thus causing instabilities.

A.3. *Vorticity solution*

Hereinafter, we follow the procedure described by Veeramony & Svendsen (2000) and adapt it to the proposed modal scheme. Let us consider the linearized equation for the vorticity field along with the boundary conditions:

$$\begin{cases} \omega_t = \nu_T(\mu^2 \omega_{xx} + \omega_{zz}), \\ \omega|_{z=\epsilon\eta} = \omega_f(x, t), \\ \omega|_{z=-h} = 0, \\ \omega|_{x=0} = \omega|_{x=L} = 0. \end{cases} \tag{A 32}$$

Differently from Veeramony & Svendsen (2000), we retain the dependence on the variable x since we need to modulate the free-surface boundary datum, ω_f, along the tank width.

https://doi.org/10.1017/jfm.2014.127 Published online by Cambridge University Press

Now, let us introduce the coordinate $y=-(\epsilon\eta-z)/d$. This new variable allows the liquid domain $(x,z)\in[0,L]\times[-h,\epsilon\eta]$ to be mapped into $(x,y)\in[0,L]\times[-1,0]$ and makes the assignment of the boundary conditions easier. Dropping the higher-order terms, the system (A 32) becomes

$$\begin{cases}\omega_t=\nu_T\left(\mu^2\omega_{xx}+\dfrac{\omega_{yy}}{h^2}\right),\\ \omega|_{y=0}=\omega_f(x,t),\\ \omega|_{y=-1}=0,\\ \omega|_{x=0}=\omega|_{x=L}=0.\end{cases}\tag{A 33}$$

It is convenient to place the free-surface boundary datum inside the vorticity equation. Thus, we set

$$\omega=\widetilde{\omega}+(y+1)\omega_f,\tag{A 34}$$

and (A 33) becomes

$$\begin{cases}\widetilde{\omega}_t=\nu_T\left(\mu^2\widetilde{\omega}_{xx}+\dfrac{\widetilde{\omega}_{yy}}{h^2}\right)+(y+1)(-\omega_{f,t}+\nu_T\mu^2\omega_{f,xx}),\\ \widetilde{\omega}|_{y=0}=\widetilde{\omega}|_{y=-1}=0,\\ \widetilde{\omega}|_{x=0}=\widetilde{\omega}|_{x=L}=0.\end{cases}\tag{A 35}$$

Since we want to express the solution as a series of modes depending on both the x and z coordinate, we need to expand $\widetilde{\omega}$, ω_f and $(y+1)$. Let us focus on the first term. To satisfy the boundary condition, one must have

$$\widetilde{\omega}=\sum_{n=1}^{+\infty}\sum_{m=1}^{+\infty}\widetilde{\Omega}_{n,m}(t)\sin(n\pi x)\sin(m\pi y)=\sum_{n\in\mathbb{R}}\frac{\mathrm{e}^{\mathrm{i}n\pi x}}{2\mathrm{i}}\sum_{m=1}^{+\infty}\widetilde{\Omega}_{n,m}(t)\sin(m\pi y).\tag{A 36}$$

Similarly, one has

$$\omega_f(x,t)=\sum_{n=1}^{+\infty}f_n(t)\sin(n\pi x)=\sum_{n\in\mathbb{R}}\frac{\mathrm{e}^{\mathrm{i}n\pi x}}{2\mathrm{i}}f_n(t),\tag{A 37}$$

and f_n is defined later. Care must be taken with the last term. Indeed, the series of sines for $(y+1)$ corresponds to the Fourier series of a sawtooth profile with a discontinuity at $y=0$. A straightforward representation of such a datum would lead to large oscillations near the discontinuity (the Gibbs phenomenon), which may also affect the solution. To avoid this issue, the term $(y+1)$ has been smoothed as follows (y being negative by definition):

$$(y+1)\rightsquigarrow(y+1)(1-\mathrm{e}^{by})\quad\text{with }b=50\tag{A 38}$$

and

$$(y+1)(1-\mathrm{e}^{by})=\sum_{m=1}^{+\infty}S_m\sin(m\pi y).\tag{A 39}$$

Substituting these expression into (A 35), we obtain

https://doi.org/10.1017/jfm.2014.127 Published online by Cambridge University Press

$$\dot{\widetilde{\Omega}}_{n,m} + \nu_T \left(\mu^2\pi^2 n^2 + \frac{\pi^2 m^2}{h^2}\right) \widetilde{\Omega}_{n,m} = -S_m(\dot{f}_n + \nu_T \mu^2 \pi^2 n^2 f_n). \tag{A 40}$$

Substituting (2.7), (A 36), (A 37) and (A 39) in (A 34), we find

$$\phi_{n,m} = \widetilde{\Omega}_{n,m} + S_m f_n, \tag{A 41}$$

and we can rewrite (A 40) as

$$\dot{\phi}_{n,m} + \nu_T \left(\mu^2\pi^2 n^2 + \frac{\pi^2 m^2}{h^2}\right) \phi_{n,m} = \left(\frac{\nu_T \pi^2 m^2}{h^2}\right) S_m f_n. \tag{A 42}$$

Assuming that the vorticity is initially zero (that is, $\phi_{n,m}(t_0) = 0$), we obtain the following solution:

$$\phi_{n,m}(t) = \left(\frac{\nu_T \pi^2 m^2}{h^2}\right) S_m \int_{t_0}^{t} f_n(\tau) \exp\left[-\nu_T \left(\mu^2\pi^2 n^2 + \frac{\pi^2 m^2}{h^2}\right)(t-\tau)\right] \mathrm{d}\tau. \tag{A 43}$$

A.3.1. *Numerical evaluation*

The time evolution of $\phi_{n,m}$ is obtained by rearranging (A 43) as follows:

$$\begin{aligned}\phi_{n,m}(t) \;=\; & \left(\frac{\nu_T \pi^2 m^2}{h^2}\right) S_m \int_{t-\Delta t}^{t} f_n(\tau) \exp\left[-\nu_T \left(\mu^2\pi^2 n^2 + \frac{\pi^2 m^2}{h^2}\right)(t-\tau)\right] \mathrm{d}\tau \\ & + \exp\left[-\nu_T \left(\mu^2\pi^2 n^2 + \frac{\pi^2 m^2}{h^2}\right)\Delta t\right] \phi_{n,m}(t-\Delta t)\,.\end{aligned} \tag{A 44}$$

Then, we just need the value of $\phi_{n,m}$ at $(t-\Delta t)$ and the value of f_n in $[t-\Delta t, t]$. Some care is required to compute the time integral. Indeed, it is not advisable to apply the trapezoidal rule directly, because we would obtain an expression for $\phi_{n,m}(t)$ that would lead to non-convergent series in m. To overcome this issue, it is convenient to expand f_n in a Taylor series as

$$f_n(\tau) = f_n(t) + \dot{f}_n(t)(\tau - t) + O(\Delta t^2) = f_n(t) + \frac{f_n(t) - f_n(t-\Delta t)}{\Delta t}(\tau - t) + O(\Delta t^2), \tag{A 45}$$

and to substitute this expression inside the above integral. For the sake of simplicity, we set

$$C = \nu_T \left(\mu^2\pi^2 n^2 + \frac{\pi^2 m^2}{h^2}\right). \tag{A 46}$$

Then, we obtain

$$\begin{aligned}&\int_{t-\Delta t}^{t} f_n(\tau)\, \mathrm{e}^{-C(t-\tau)}\, \mathrm{d}\tau \\ &\quad = f_n(t)\frac{(1-\mathrm{e}^{-C\Delta t})}{C} - \left[\frac{f_n(t) - f_n(t-\Delta t)}{\Delta t}\right]\left[\frac{1-(1+C\Delta t)\mathrm{e}^{-C\Delta t}}{C^2}\right] + O(\Delta t^3).\end{aligned} \tag{A 47}$$

https://doi.org/10.1017/jfm.2014.127 Published online by Cambridge University Press

This result is somewhat similar to the trapezoidal rule and has the same order of accuracy.

REFERENCES

ANTUONO, M., BOUSCASSE, B., COLAGROSSI, A. & LUGNI, C. 2012 Two-dimensional modal method for shallow-water sloshing in rectangular basins. *J. Fluid Mech.* **700**, 419–440.

ANTUONO, M. & BROCCHINI, M. 2013 Beyond Boussinesq-type equations: semi-integrated models for coastal dynamics. *Phys. Fluids* **25**, 016603.

ANTUONO, M. & COLAGROSSI, A. 2013 The damping of viscous gravity waves. *Wave Motion* **50**, 197–209.

ANTUONO, M., COLAGROSSI, A., MARRONE, S. & LUGNI, C. 2011 Propagation of gravity waves through an SPH scheme with numerical diffusive terms. *Comput. Phys. Commun.* **182**, 866–877.

ARDAKANI, H. A. & BRIDGES, T. J. 2012 Shallow-water sloshing in vessels undergoing prescribed rigid-motion in two dimensions. *Eur. J. Mech.* B*/Fluids* **31**, 40–43.

BOUSCASSE, B., ANTUONO, M., COLAGROSSI, A. & LUGNI, C. 2013 Numerical and experimental investigation of nonlinear shallow water sloshing. *Intl J. Nonlinear Sci. Numer. Simul.* **14** (2), 123–138.

BREDMOSE, H., BROCCHINI, M., PEREGRINE, D. H. & THAIS, L. 2003 Experimental investigation and numerical modelling of steep forced water waves. *J. Fluid Mech.* **490**, 217–249.

CHESTER, W. & BONES, J. A. 1968 Resonant oscillations of water waves. II. Experiment. *Proc. R. Soc. Lond.* A **306**, 23–29.

COX, D. T., KOBAYASHI, N. & OKAYASU, A. 1995 Experimental and numerical modelling of surf zone hydrodynamics. *Tech. Rep.* University of Delaware.

FALTINSEN, O. M., LANDRINI, M. & GRECO, M. 2004 Slamming in marine applications. *J. Engng Maths* **48**, 187–217.

FALTINSEN, O. M., ROGNEBAKKE, O. F., LUKOVSKY, I. A. & TIMOKHA, A. N. 2000 Multidimensional modal analysis of nonlinear sloshing in a rectangular tank with finite water depth. *J. Fluid Mech.* **407**, 201–234.

FALTINSEN, O. M. & TIMOKHA, A. N. 2001 An adaptive multimodal approach to nonlinear sloshing in a rectangular tank. *J. Fluid Mech.* **432**, 167–200.

FALTINSEN, O. M. & TIMOKHA, A. N. 2002 Asymptotic modal approximation of nonlinear resonant sloshing in a rectangular tank with small fluid depth. *J. Fluid Mech.* **470**, 319–357.

FALTINSEN, O. M. & TIMOKHA, A. N. 2009 *Sloshing*. Cambridge University Press.

HILL, D. F. 2003 Transient and steady-state amplitudes of forced waves in rectangular basins. *Phys. Fluids* **39** (6), 1576–1587.

LAMB, H. 1945 *Hydrodynamics*. Cambridge University Press.

LEPELLETIER, T. G. & RAICHLEN, F. 1988 Nonlinear oscillations in rectangular tanks. *J. Engng Maths* **114** (1), 1–23.

OLSEN, H. & JOHNSEN, K. 1975 Nonlinear sloshing in rectangular tanks: a pilot study on the applicability of analytical models. *Tech. Rep.* 74-72-5, vol. 2. Det Norske Veritas (DNV), Hvik, Norway.

VEERAMONY, J. & SVENDSEN, I. A. 2000 The flow in surf-zone waves. *Coast. Engng* **39**, 93–122.

https://doi.org/10.1017/jfm.2014.127 Published online by Cambridge University Press